Influence of Meso-Scale Parameters on the Large-Deformation Behaviour of Ultra-Thin Woven Fibre Composites

W.M.H.G.L.C.B. Weerasekara

248066J

Degree of Master of Science

Department of Civil Engineering

University of Moratuwa
Sri Lanka

February 2026

Influence of Meso-Scale Parameters on the Large-Deformation Behaviour of Ultra-Thin Woven Fibre Composites

W.M.H.G.L.C.B. Weerasekara

248066J

Thesis submitted in partial fulfilment of the requirements for the degree of Master of Science in Civil Engineering

Department of Civil Engineering

University of Moratuwa
Sri Lanka

February 2026

Declaration

I declare that this is my own work and this thesis does not incorporate without acknowledgement any material previously submitted for a Degree or Diploma in any other University or institute of higher learning and to the best of my knowledge and belief it does not contain any material previously published or written by another person except where the acknowledgement is made in the text.

Also, I hereby grant to University of Moratuwa the non-exclusive right to reproduce and distribute my thesis, in whole or in part in print, electronic or other medium. I retain the right to use this content in whole or part in future works (such as articles or books).

.... Date : 05/02/2026

W.M.H.G.L.C.B. Weerasekara

The above candidate has carried out research for the Masters thesis under my supervision.

.... Date : 07/02/2026

Prof. H.M.Y.C. Mallikarachchi

.... Date : 07/02/2026

Dr. H.M.S.T. Herath

Abstract

Ultra-thin woven composite laminates are widely used in deployable space structures, in which they experience large curvatures during both folding and deployment. Under such conditions, these laminates exhibit pronounced non-linear bending behaviour characterised by a progressive reduction in stiffness. Accurate prediction of this response is essential for reliable structural design. This study presents a comprehensive numerical framework to investigate the non-linear bending behaviour of ultra-thin two-ply plain-weave composite laminates using a representative unit cell based homogenisation approach.

A multi-scale finite element model was developed that integrates an explicit geometric representation of the woven architecture, geometric non-linearity associated with large deformations, strain-dependent material non-linearity of tows and cohesive traction–separation behaviour at tow–tow and inter-ply interfaces. The proposed framework enables direct evaluation of the laminate moment–curvature response and extraction of homogenised stiffness parameters.

The numerical predictions show strong agreement with experimental results over the full range of curvatures investigated. The model accurately captures the progressive reduction in bending stiffness with increasing curvature and reveals that this degradation arises from the combined influence of geometric effects, inter-tow interactions and material non-linearity of carbon fibres. At moderate curvatures, stiffness reduction is dominated by geometric mechanisms, including tow flattening, cross-sectional deformation and neutral-axis shift. At higher curvatures, cohesive damage and micro-slipping between adjacent tows become the primary contributors.

Inclusion of resin layers between plies was shown to be critical for accurate stiffness prediction, as the resin constrains inter-ply motion and increases the number of effective contact interfaces, enabling close replication of experimentally measured initial bending stiffness. A comparative investigation of fibre in-phase and out-of-phase stacking arrangements demonstrated that ply alignment has a significant influence on bending stiffness.

Overall, the proposed homogenisation framework provides a robust and physically grounded tool for predicting the complex bending behaviour of ultra-thin woven composites. In addition to reproducing experimental responses with high accuracy, the approach enables extraction of homogenised ABD stiffness matrices suitable for macro-scale modelling and design of deployable composite space structures.

Keywords : *cohesive behaviour, damage criterion, non-linear bending behaviour, representative unit cell, ultra-thin woven fibre composites*

Dedication

To my parents and brother, whose support made all of this possible.

Acknowledgement

First and foremost, I wish to express my sincere and profound gratitude to my supervisors, Prof. Chinthaka Mallikarachchi and Dr. Sumudu Herath, for providing me with the invaluable opportunity to undertake this research under their expert supervision. Their exceptional technical expertise, insightful guidance and unwavering support were instrumental throughout the course of this study and continually motivated me to strive for the highest academic standards. This research would not have been possible without their dedicated mentorship and commitment.

I would also like to extend my sincere appreciation to Prof. Priyan Dias for the constructive comments and valuable advice provided during progress reviews. His insightful suggestions encouraged critical thinking and inspired alternative perspectives in addressing complex research challenges.

My special appreciation is extended to Uditha Weerasinghe for initiating the incorporation of material non-linearity into meso-scale modelling, and to Eroshan Gamage for compiling and summarising the experimental results referenced in this study. I am also grateful to Chamika Wanasinghe and Nirodha Sandaruwan for their consistent support and engaging technical discussions, which significantly enriched the quality of this research.

I would like to acknowledge with gratitude the academic staff of the Department of Civil Engineering at the University of Moratuwa for their encouragement, guidance, and support throughout my academic journey.

I am deeply thankful for the financial support provided by the Indo–Sri Lanka Joint Research Programme, without which the successful completion of this research would not have been possible.

Finally, I gratefully acknowledge all those who, in any capacity, contributed to the successful completion of this work.

Contents

List of Figures

List of Tables

Nomenclature

Δl	Nominal weave length, mm
δ'	Traction separation, mm
γ	Engineering shear strain, mm/mm
κ	Mid-plane curvature, 1/mm
ν	Poisson's ratio
ϕ	Rotation angle change, Rad
ρ	Density, kg/m^3
θ	Initial angle, Rad
ε	Mid-plane strain, mm/mm
ε_m	Meso-scale finite strain tensor, mm/mm
A_{ij}	Coefficients of upper-left 3×3 sub-matrix of ABD, N/mm
A_{tow}	Average cross-sectional area of a tow, mm^2
B_{ij}	Coefficients of upper-right 3×3 sub-matrix of ABD, N
C_M	Macro-scale material constitutive tensor
C_m	Meso-scale material constitutive tensor
d	Major axis diameter, mm
D_{ij}	Coefficients of lower-right 3×3 sub-matrix of ABD, Nmm
E	Elastic modulus, N/mm^2
F	Nodal force matrix
G	Shear modulus, N/mm^2

h Minor axis diameter, mm

K Traction stiffness, MPa/mm

k Non-dimensional parameter

l Arm length, mm

l_s Free length of the specimen, mm

M Moment per unit length stress resultant, Nmm/mm

N Force per unit length stress resultant, N/mm

n_m Normal vectors

P Applied load, N

P_i Control points

P_M Macro-scale finite stress tensor, N/mm^2

r Moment arm length, mm

s Non-dimensional path parameter

t Traction stress, MPa

t_{tow} Average tow thickness, mm

U Nodal displacement matrix

u Translations in x direction, mm

U_M Macro-scale deformation gradient, mm

U_m Meso-scale deformation gradient, mm

v Translations in y direction, mm

V_f Fibre volume fraction

W Areal weight, g/m^2

w Translations in z direction, mm

w_m Meso-scale micro-fluctuations

w_{tow} Average tow width, mm

X_M Position vector in reference configuration

x_m Position vector in deformed configuration

Chapter 1

Introduction

1.1 Overview

Ultra-thin woven composites are increasingly employed across aerospace, transport and manufacturing industries owing to their high strength and stiffness-to-weight ratios, tailorability, damage tolerance and ease of handling and fabrication. These materials have gained particular prominence in the development of lightweight deployable structures, which are seen as attractive alternatives to conventional rigid structures, especially in aerospace applications where storage efficiency is a critical design constraint.

Constraints imposed by launch vehicle payload capacity and stowage volume play a decisive role in the design of large-scale space structures such as solar sails, solar arrays and reflector antennas. However, the operational dimensions of such structures often far exceed those of the launchers. To address this, the concept of deployable structures has emerged in which large structures can be compactly stowed during launch and later deployed to their full operational configuration once in orbit. Various deployable mechanisms have been developed to achieve this, including inflatable structures, mechanically jointed systems, motorised assemblies and deployable booms. Booms constructed from woven fibre composites harness the strain energy stored during folding to achieve self-deployment, eliminating the need for additional motorised systems. In such systems, self-deployment is commonly achieved by elastically deforming the structural elements to store strain energy, which is later released during deployment.

For ultra-thin woven composites to be successfully utilised and optimised in such applications, an accurate understanding of their material behaviour and failure mechanisms is essential. However, modelling these materials remains challenging due to their complex internal architecture, which involves multiple hierarchical scales from tows to plies to laminates. Existing predictive models often require simplifications and are subject to considerable uncertainties, which accumulate across hierarchical levels and compromise the reliability of performance estimates.

1.2 Recent Developments

Deployable structures have already been utilised in several space missions, and a variety of novel structural architectures employing this approach have been proposed for future applications.

A landmark example is the antenna used in the Mars Advanced Radar for Subsurface and Ionospheric Sounding (MARSIS) mission, designed to look below the surface of Mars, most notably to look for water [1]. The MARSIS antenna comprises a dipole structure made from S-glass/Kevlar composite booms, each 20 m in length and 3.8 cm in diameter, along with a 7 m monopole boom. These elements were folded into 1.5 m sections and stowed in a compact cradle as shown in Figure 1.1, exemplifying the efficiency and compactness of deployable composite booms in real-world applications.

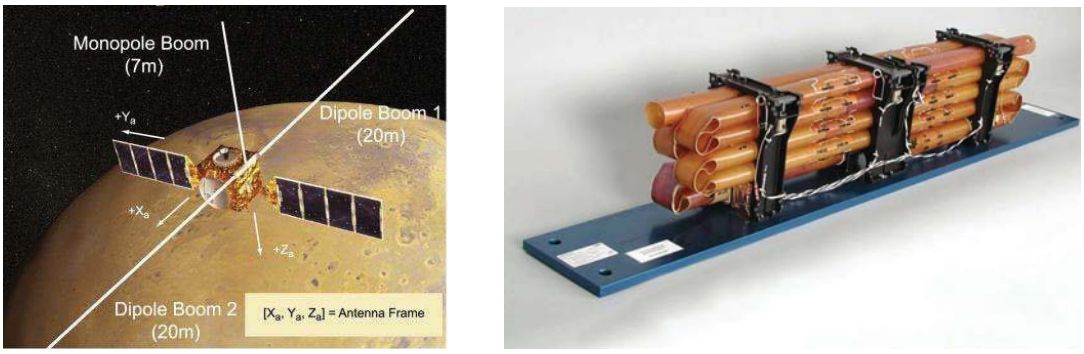

Figure 1.1: MARSIS booms (Courtesy: Astro Aerospace)

Thin laminates made from woven fibre composites are capable of sustaining large bending curvatures before failure, providing a high degree of flexibility that is particularly advantageous for deployable space structures, where components must be compactly stowed for launch [2, 3, 4]. More recently, the Advanced Composite Solar Sail System (ACS3) mission developed by the National Aeronautics and Space Administration (NASA) has provided experimental validation of novel deployable composite boom technologies in the space environment [5]. The mission successfully demonstrated both the compact packaging and autonomous deployment of ultra-thin composite booms in conjunction with an 80 m^2 solar sail, underscoring the increasing maturity of such materials for future space missions requiring scalable and mass-efficient deployable systems. As illustrated in Figure 1.2, the mission utilised ultra-thin plain-weave carbon fibre composite booms that were rolled and compactly stowed during launch and then autonomously unrolled in space to deploy the sail. The successful deployment of the ACS3 sail demonstrated that ultra-thin composite materials can operate reliably under space conditions while achieving high packaging efficiency and structural precision.

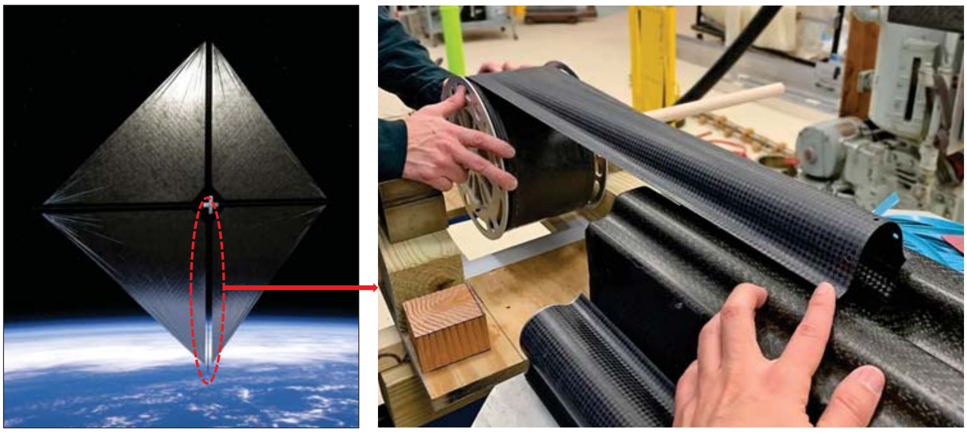

Figure 1.2: NASA's ACS3 mission (Courtesy: NASA)

1.3 Non-linear Bending Behaviour at Large Curvatures

As discussed in Section 1.2, these deployable booms undergo significant deformation during both the folding and deployment. An experimental investigation on two-ply plain weave T300-1k/Hexcel 913 composites, conducted by Mallikarachchi and Pellegrino [6], reported a 34% reduction in bending moment near failure curvatures when compared to extrapolated predictions based on initial stiffness, highlighting the need to study the non-linear bending behaviour under large curvatures. However, the experimental results in that study were obtained from two separate tests: the initial stiffness was measured using a four-point bending test, while the failure response was derived from a platen folding test. In contrast, Gamage [7] attempted to characterise the complete bending response from initial stiffness to failure using the Column Bending Test (CBT) on a two-ply plain weave T300-1k/PMT-F4 epoxy laminate and reported a 32% reduction in bending moment near failure curvatures.

1.4 Challenges

Given that these deployable structures are critical components in space missions, typically valued in the range of millions of US dollars, it is essential to accurately identify and understand their mechanical behaviour before deployment. The highly non-linear geometric deformations and dynamic snapping events that occur during folding and deployment make physical experimentation both challenging and resource-intensive. In addition, environmental factors such as gravity and air drag, which are unavoidable under terrestrial conditions, significantly influence experimental results involving deployable booms based on stored energy. The time-consuming, costly and often challenging nature of physical testing further underscores the need for alternative methods, particularly in the context of design optimisation, where multiple iterative cycles are typically required.

Classical Lamination Theory (CLT) has long been employed for the analysis and design of laminated composite structures and has proven effective for unidirectional laminae. However, its direct application to woven fibre composites is limited due to several underlying assumptions which are not valid for woven fibre composites, particularly in the case of ultra-thin laminates with only a few plies, where the actual fibre architecture introduces significant variation through the thickness [8]. Previous studies have attempted to extend CLT to woven systems. For instance, Le Page et al. [9] and Naik [10] applied analytical methods based on CLT, achieving reasonable accuracy in predicting in-plane properties. However, these models failed to accurately capture flexural behaviour, especially in ultra-thin woven fibre composites. Notably, Karkkainen and Sankar [11], as well as Soykasap [12], reported that the direct use of CLT significantly overestimated the bending stiffness, by as much as 300% and 400%, respectively.

To address these limitations, virtual testing methods have gained attention, with numerical simulations being a primary tool for evaluating the mechanical response of thin-walled composite booms. Commercial finite element software packages are well-suited for these applications, as they can accommodate the complex contact interactions and geometric discontinuities involved. Among many numerical approaches available in the literature, the multi-scale modelling approach has been successfully utilised in the design of deployable space structures [13, 14].

1.5 Scope and Aim

The primary aim of this research is to investigate the mechanisms governing the non-linear mechanical response of ultra-thin woven fibre composites subjected to large deformations. In particular, the study seeks to identify the geometric, material and interfacial mechanisms that contribute to the progressive reduction in bending stiffness at high curvatures. To achieve this objective, a meso-mechanical representative unit cell (RUC) model was developed to accurately capture the flexural behaviour of woven laminates under high-curvature bending. The resulting framework is intended to support the design and numerical simulation of ultra-thin deployable booms manufactured from woven composite laminae within a multi-scale modelling context.

The scope of the work focuses on a two-ply plain-weave composite laminate composed of T300-1k carbon fibre tows embedded in a PMT-F4 epoxy resin. A suitable repeating geometry was first identified to represent the woven architecture of the laminate. Based on geometric parameters obtained from X-ray Computed Tomography (XRCT) characterisation [7], a detailed micromechanical RUC model was constructed using the TexGen finite element pre-processor. The resulting mesh was subsequently imported into the commercial finite element package Abaqus, where homogenised laminate stiffness properties were evaluated.

To accurately represent tow–tow and inter-ply interactions under large curvature bending, cohesive interaction laws with damage evolution were introduced at relevant contact interfaces. These cohesive models enable simulation of interfacial degradation mechanisms such as tow separation and micro-slipping, which are known to play a significant role in bending stiffness reduction at high curvatures. In parallel, a strain-dependent non-linear constitutive model was implemented at the constituent level to account for material non-linearity of the fibre tows, allowing its influence on the overall bending response to be quantified.

In addition, a phase sensitivity analysis was performed by considering fibre in-phase and out-of-phase stacking configurations. This analysis was undertaken to assess the influence of ply alignment on the homogenised bending stiffness and non-linear moment–curvature response. The results provide insight into the variability in mechanical behaviour arising from ply positioning, highlighting the sensitivity of ultra-thin woven laminates to manufacturing-induced phase differences.

Through the integration of geometric non-linearity, material non-linearity, cohesive interface behaviour and stacking phase effects within a unified RUC-based homogenisation framework, the proposed methodology successfully captures the complex non-linear bending response of ultra-thin woven fibre composites. The outcomes of this work provide both accurate predictive capability and mechanistic insight, offering a robust foundation for the design, analysis, and optimisation of future deployable composite space structures.

1.6 Chapter Organisation

This thesis consists of seven chapters. Following this introductory chapter, Chapter 2 provides an overview of the literature on stored-energy deployable space structures, woven fibre composites, experimental studies on the bending behaviour of woven fibre composites, analytical approaches and previous studies on characterising their flexural behaviour numerically. Chapter 3 describes the specific material used in this study. The geometric and material properties are presented, along with the idealisations employed in the numerical modelling. Chapter 4 details the construction of the RUC in Abaqus using the geometry exported from TexGen. This chapter covers the geometric modelling of the RUC, boundary conditions, cohesive interactions, formation of the constitutive relationship and the USDFLD subroutine used to model material non-linearity. Chapter 5 presents the results, while Chapter 6 concludes the thesis and provides suggestions for future research directions.

Chapter 2

Literature Review

This chapter reviews the existing literature on stored-energy deployable structures and the analysis of woven fibre composites. It begins with a discussion of woven fibre composites in deployable space structures, followed by an examination of the non-linear bending behaviour of woven fibre composites under large curvatures. The subsequent section provides an overview of the analytical approaches used in this field. Finally, the chapter concludes with a review of multi-scale modelling techniques and their relevance to the present study.

2.1 Woven Fibre Composites in Deployable Space Structures

Deployable structures are increasingly being utilised in space missions due to their lightweight construction and high reliability. Unlike traditional mechanical actuators and motors, deployable booms do not rely on external power sources. Instead, they harness the strain energy stored during the folding process to enable self-deployment. This characteristic renders them particularly suitable for large, high-precision space systems where minimal mass and mechanical simplicity are of paramount importance.

Many space systems employ deployable booms to extend and support peripheral components, including large antenna reflectors, solar arrays for power generation, and solar sails for propulsion. Various organisations, including NASA and the German Aerospace Centre (DLR), have developed different types of deployable structures that utilise stored strain energy. These structures, which may have either open or closed cross-sections, are typically categorised into four primary types: Tape Spring booms, Triangular Rollable and Collapsible (TRAC) booms, Storable Tubular Extendable Membrane (STEM) booms, and Collapsible Tubular Mast (CTM) booms [15]. In some systems, tape spring mechanisms have been further integrated into monolithic designs, where the boom and its deployment mechanism form a single continuous structure. For example, in large deployable antennas such as those used in the MARSIS mission, composite tubes are slotted at regular intervals to create integral tape spring hinges [1]. While early tape springs were manufactured from metallic alloys, more recent designs employ fibre-reinforced composites, capitalising on their high stiffness-to-weight ratio and tunable material properties.

As the name suggests, woven fibre composites are composed of two fundamental constituents: the fibres, which are responsible for load transfer and the resin, which binds the individual fibres together. A bundle of continuous filaments made from materials such as carbon, glass or aramid is referred to as a tow. These tows are interlaced to form a woven fabric, providing greater intra-laminar strength than unidirectional laminae. A variety of weave patterns, ranging from simple plain weaves to more complex triaxial weaves, can be employed to meet specific mechanical and structural requirements. These composites consist of two principal sets of interlaced tows that serve as reinforcement. Depending on the weaving direction, they are referred to as the warp and fill tows. The warp tows are aligned along the length of the fabric, commonly known as the machine direction, while the fill tows run perpendicular to them. The fabric is produced on a loom by interlacing these tows at specific angles. A schematic representation of the components of a plain-weave fabric is shown in Figure 2.1.

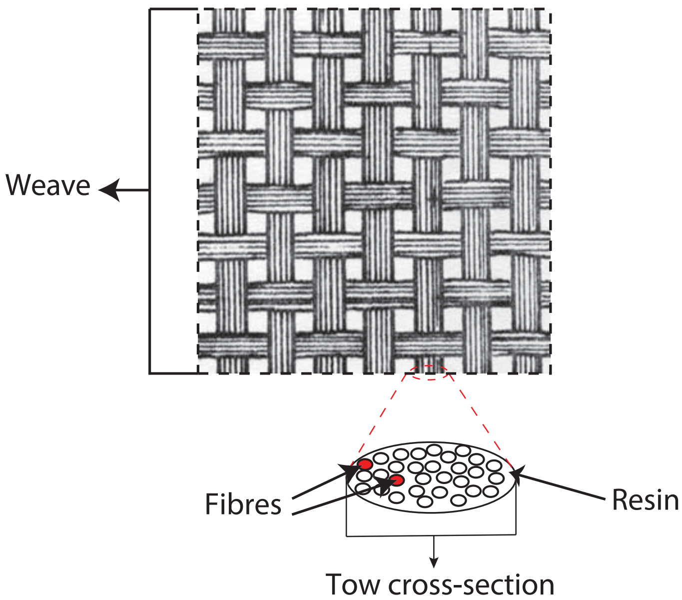

Figure 2.1: Schematic of a plain-weave fabric

2.2 Non-linear Bending Behaviour of Woven Fibre Composites at Large Curvatures

Ultra-thin woven fibre composites are part of a broader class of fibre-reinforced materials known as high-strain composites (HSCs), which are specifically engineered to sustain bending strains exceeding 1% [16]. A considerable body of research has been devoted in recent years to understanding the mechanical behaviour and potential applications of thin woven fibre composites. In the context of strain-energy deployable structures, their primary mode of deformation is bending. Accordingly, characterising their bending response is critical for the design of deployable structural systems.

Mallikarachchi and Pellegrino [6] conducted a comprehensive experimental investigation on a two-ply T300-1k/Hexcel 913 plain weave laminate to characterise the behaviour of ultra-thin woven fibre composites. The study involved various mechanical tests, including tensile, compression, shear, bending, twisting and biaxial loading. To evaluate the bending response, a four-point bending test was employed as shown in Figure 2.2, which experiences a uniform bending moment within the region between the two loading points. The initial bending stiffness was determined by analysing both loading and unloading phases. The results indicated a mean bending stiffness of 37.55 Nmm with a standard deviation of 5.54 Nmm.

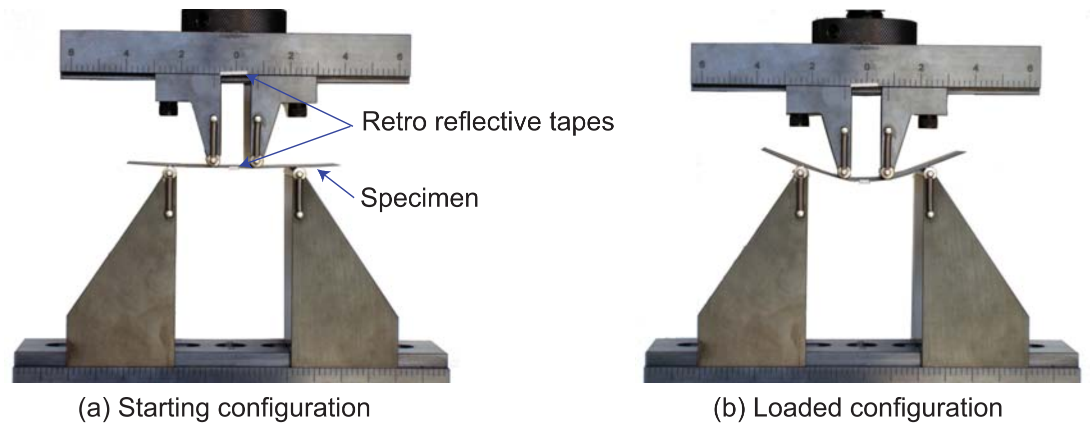

Figure 2.2: Four-point bending test setup [17]

However, due to the broad elastic deformation range of ultra-thin laminates, the four-point bending test is not suitable for determining the failure point. Consequently, a platen folding test was conducted to assess failure as presented in Figure 2.3. From a series of tests, the measured failure moment was

5.068 ± 0.293 Nmm/mm, occurring at a curvature of 0.203 ± 0.01 mm^{-1} [6]. But, when the initial bending stiffness determined from the four-point bending test was extrapolated to the same failure curvature of 0.203 mm^{-1}, it yielded a significantly higher value of 7.622 Nmm/mm. According to the results, there is a 34% reduction in bending moment near failure curvatures.

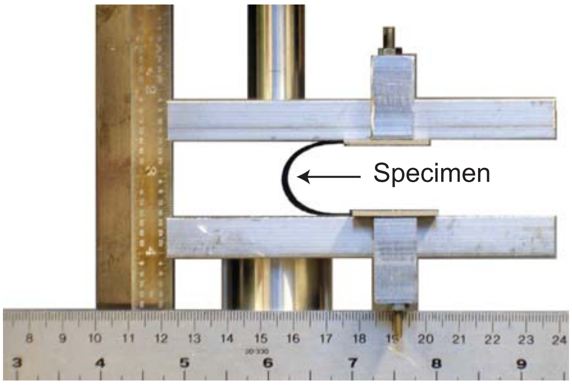

Figure 2.3: Platen folding test setup [17]

Recently, Gamage [7] attempted to characterise the complete bending response from initial stiffness to failure using CBT on a two-ply plain weave T300-1k/PMT-F4 epoxy laminate. CBT is chosen in this study for its capability to capture the full range of non-linear bending behaviour in a single test, while also replicating a pure bending stress state up to failure near the centre of the coupon. Figure 2.4 presents the experimental setup used in this study.

Figure 2.5 shows a schematic diagram of CBT indicating the parameters, arm length, l, free length of the specimen, l_s, initial angle, θ, applied load, P, clevis displacement, δ, moment arm length, r, and arm rotation angle change, ϕ. Specimens with dimensions of 50 mm × 20 mm, were clamped vertically between two counterbalanced rigid arms to minimise gravitational effects. These arms were pinned to U-shaped clevises, which were in turn connected to the loading heads of an Instron 5569 universal testing machine (UTM). An eccentric offset between the loading axis and the specimen introduced an initial angle, thereby generating a bending moment as the clevises converged. The lower arm was fixed to the UTM base, while the upper arm connected to a 10 N load cell was displaced downward at a constant rate of 0.17 mm/s (10 mm/min), producing quasi-static conditions. Load and displacement data were recorded at intervals of 0.02 s.

Full-field deformation was captured using a VIC-3D Digital Image Correlation (DIC) system. The moment–curvature response was obtained from the load and displacement measurements recorded during testing. To generate smooth and

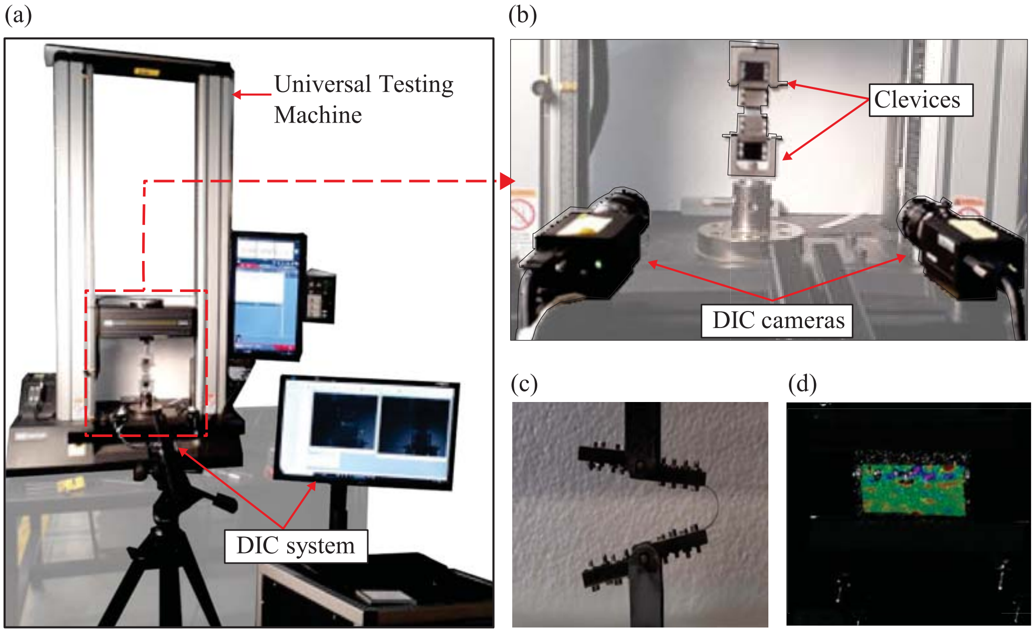

Figure 2.4: CBT setup: (a) Overall experimental setup, (b) Zoomed view of test region, (c) Side view of specimen during bending, (d) DIC measurements superimposed on deformed specimen [7]

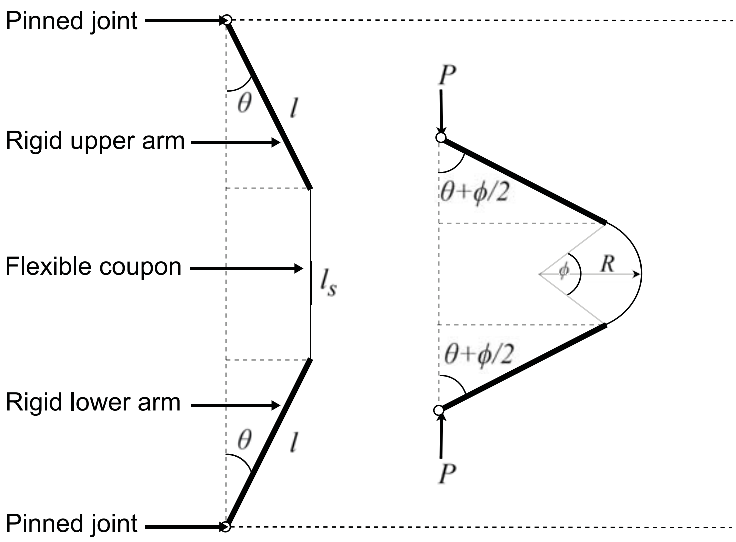

Figure 2.5: Schematic diagram of CBT

continuous curves, a third-degree polynomial was fitted to the results of each test as presented in Equation 2.1, with the corresponding coefficients listed in Table 2.1.

$$F(x) = Ax^3 + Bx^2 + Cx \tag{2.1}$$

Table 2.1: Coefficients of fitted third degree polynomial for each trial

Specimen ID	A	B	C	Failure curvature (mm^{-1})
PW-SP1	-45.82	-42.96	36.03	0.1854
PW-SP2	245.7	-142.2	42.87	0.1501
PW-SP3	100.1	-81.41	37.08	0.1905
PW-SP4	66.99	-74.73	39.55	0.1883
PW-SP5	80.44	-92.39	45.24	0.1557
PW-SP6	-118.4	-39.47	39.82	0.1536
PW-SP7	96.81	-95.56	43.46	0.1564
PW-SP8	28.62	-70.15	34.03	0.1809

The moment–curvature responses for all trials are presented in Figure 2.6, where the slope of each curve represents the bending stiffness, D_{11}, as a function of curvature. The averaged moment–curvature response, including standard deviations, is shown in Figure 2.7. Based on the CBT results, the initial bending stiffness was determined to be 39.76 $\pm$ 3.92 Nmm. Additionally, near the failure curvatures, the bending moment exhibited a mean reduction of 32% relative to the extrapolated initial stiffness.

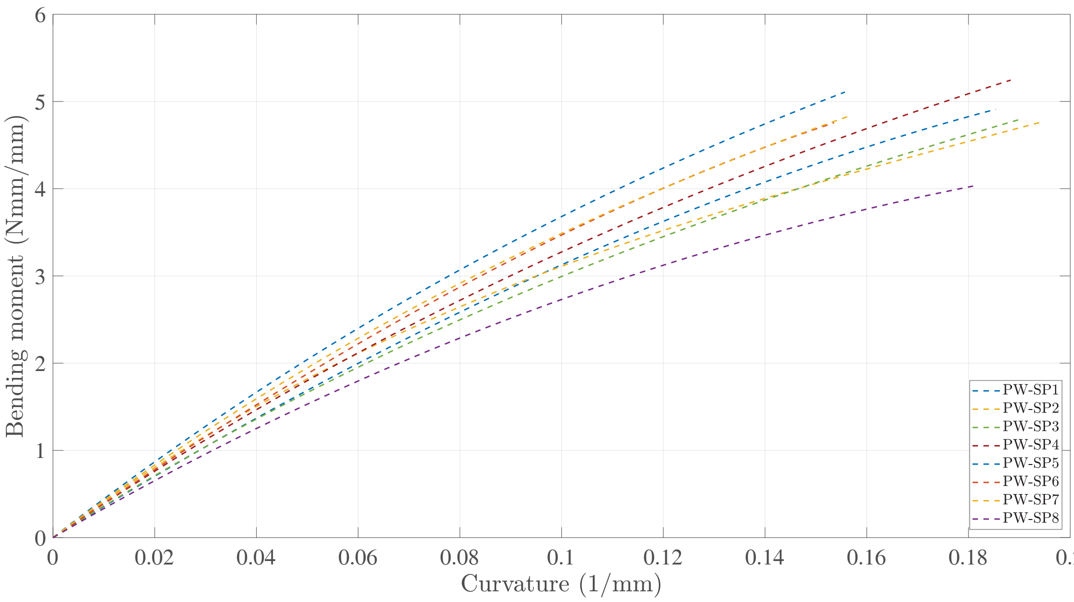

Figure 2.6: Individual moment-curvature responses [7]

In addition to these two detailed experimental investigations, several other studies have also indicated that thin woven composites exhibit non-linear bending behaviour at high curvatures [18, 19, 20], emphasising the need to investigate their mechanical response under large curvatures.

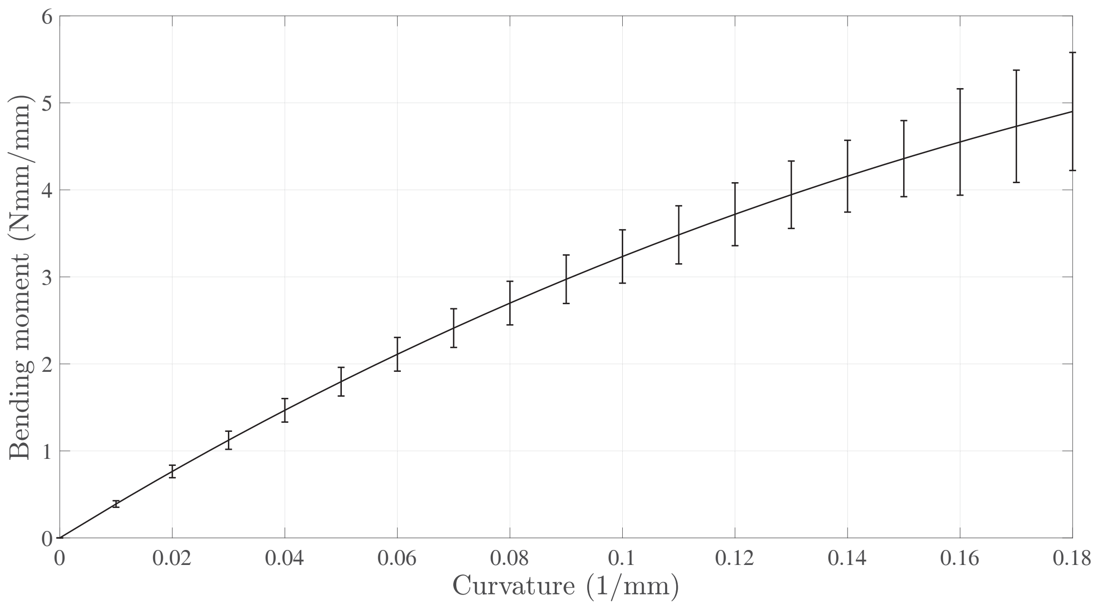

Figure 2.7: Mean moment-curvature response of specimens with standard deviations [7]

2.3 Analytical Approaches

A considerable number of analytical studies based on CLT have been conducted on woven fibre composites to investigate their mechanical properties. CLT is founded on the well-established Kirchhoff-Love hypothesis for shells, which itself is derived from the Euler-Bernoulli beam theory. Consequently, it inherits the key assumptions of these foundational models. One of the principal assumptions is that the middle surface of the laminate remains straight and normal to the deformed mid-surface during bending or stretching. This implies that transverse shear strains vanish, i.e., $\gamma_{xz} = \gamma_{yz} = 0$. Additionally, it is assumed that the bonding between laminae is infinitesimally thin and perfectly rigid, prohibiting inter-laminar slip, and that the thickness of each individual lamina remains constant.

In CLT, the analysis of a laminate follows a systematic procedure. First, each lamina is individually analysed by relating its in-plane stresses to in-plane strains and out-of-plane curvatures. These relationships are then integrated through the laminate thickness to compute the resultant forces and moments. This process results in the formulation of the ABD matrix, a standard 6×6 constitutive matrix that characterises the overall mechanical behaviour of the laminate. The compact form of this matrix is presented in Equation 2.2.

$$\left\{ \begin{array}{c} N \\ M \end{array} \right\} = \begin{pmatrix} A & B \\ B & D \end{pmatrix} \left\{ \begin{array}{c} \varepsilon \\ \kappa \end{array} \right\} \tag{2.2}$$

Here, N refers to the in-plane force resultants, M to the out-of-plane moment resultants, and ε and κ to the in-plane strains and out-of-plane curvatures, respectively. The ABD matrix consists of three sub-matrices: A, B, and D, each comprising nine components. The A matrix defines the relationship between in-plane force resultants and strains, whereas the D matrix relates out-of-plane moment resultants to curvatures. The B matrix captures the coupling between extensional and bending responses. An expanded version of the ABD matrix, showing the links between in-plane forces, out-of-plane moments, in-plane strains, and out-of-plane curvatures, is given in Equation 2.3. The directions x and y correspond to the two principal orientations of the fibre tows.

$$\left\{ \begin{array}{c} N_x \\ N_y \\ N_{xy} \\ -- \\ M_x \\ M_y \\ M_{xy} \end{array} \right\} = \begin{pmatrix} A_{11} & A_{12} & A_{16} & | & B_{11} & B_{12} & B_{16} \\ A_{21} & A_{22} & A_{26} & | & B_{21} & B_{22} & B_{26} \\ A_{61} & A_{62} & A_{66} & | & B_{61} & B_{62} & B_{66} \\ -- & -- & -- & -- & -- & -- & -- \\ B_{11} & B_{21} & B_{61} & | & D_{11} & D_{12} & D_{16} \\ B_{12} & B_{22} & B_{62} & | & D_{21} & D_{22} & D_{26} \\ B_{16} & B_{26} & B_{66} & | & D_{61} & D_{62} & D_{66} \end{pmatrix} \left\{ \begin{array}{c} \varepsilon_x \\ \varepsilon_y \\ \gamma_{xy} \\ -- \\ \kappa_x \\ \kappa_y \\ \kappa_{xy} \end{array} \right\} \tag{2.3}$$

Due to the inherent geometry and interlacing patterns of tows in woven textiles, many of the fundamental assumptions underlying CLT do not hold for such materials. Specifically, a lamina composed of woven fibres does not maintain a constant thickness across its surface. Since the calculation of resultant forces and moments in CLT relies on integration through the laminate thickness, any variation in thickness can substantially affect the bending stiffness, notably the components of the D matrix. Karkkainen and Sankar [11] applied CLT to analyse two-ply plain weave composites and observed that it overestimated the bending stiffness by approximately 300%. Similarly, Soykasap [12] reported that CLT produced errors of up to 400% in predicting maximum bending stiffness. These findings, supported by micromechanical principles, clearly demonstrate that CLT is inadequate for accurately predicting the flexural behaviour of ultra-thin woven fibre composites.

2.4 Numerical Studies

Numerical studies have gained preference over physical experiments for investigating ultra-thin woven composites. This shift is largely due to the availability of advanced computational techniques that enable the incorporation of realistic architectural structures and accurate material properties into simulations. Compared to classical analytical methods, numerical models offer significant advantages. They allow for the realistic representation of complex composite geometries using Computer-Aided Design (CAD) tools. Moreover, finite element simulations provide detailed insights into stress and strain distributions within the composite, making them highly suitable for predicting failure [21].

2.4.1 Multi-Scale Modelling Approach

Multi-scale modelling technique has been utilised to predict macroscopic properties of the composite by linking the underlying micro-structure through volume averaging of field variables, conserving consistency. The schematic shown in Figure 2.8 outlines a methodology for characterising the mechanical behaviour of deployable booms using an RUC of the textile composite. The approach is iterative, where the material response of the boom is continuously updated based on the analysis results, specifically the displacement and rotational parameters derived from the deformed configuration of the boom [22].

To effectively employ the multi-scale modelling technique, it is crucial to understand the micromechanical behaviour of woven fibre composites. Different application-specific hierarchical scales are employed in various analyses, with the most common scales used to analyse woven composites being the micro-scale, meso-scale and macro-scale [23, 24, 25].

2.4.2 Micro-Mechanical Modelling of Woven Textiles

Various efforts have been made to idealise the RUC for such materials. The RUC represents the repeating pattern of the weave geometry at the meso-scale level of textiles. Its configuration is determined by the arrangement of the tows and the stacking of the plies. Figure 2.9 illustrates RUCs corresponding to plain weave and triaxial weave geometries.

Karkkainen and Sankar [11] developed a direct micro-mechanical finite element model for a plain weave lamina. This model was among the first to

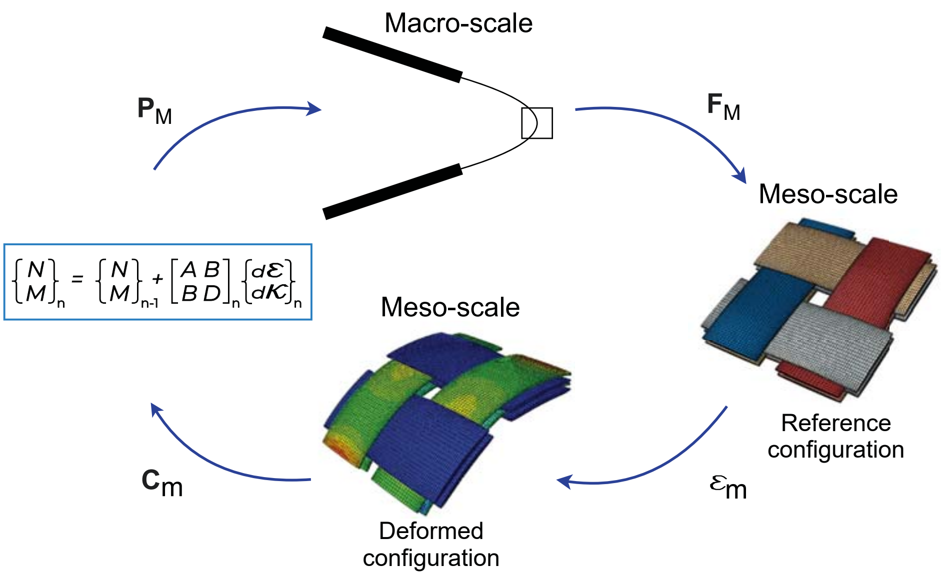

Figure 2.8: Multi-scale modelling approach: F_M, ϵ_m, C_m and P_M stand for macro-scale deformation gradient, meso-scale finite strain tensor, meso-scale material constitutive tensor and macro-scale finite stress tensor, respectively

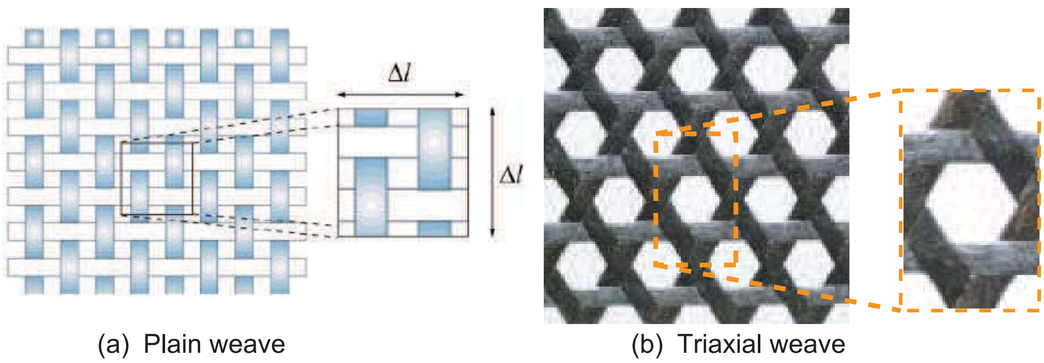

Figure 2.9: Identification of RUC in woven textiles

incorporate bending effects by employing the Kirchhoff–Love shell theory for homogenisation. Additionally, boundary conditions were implemented to reflect the repeating nature of the RUC. As a result, the constitutive relationship was expressed in terms of the ABD matrix, a standard representation for laminated composites. Figure 2.10 illustrates their proposed RUC.

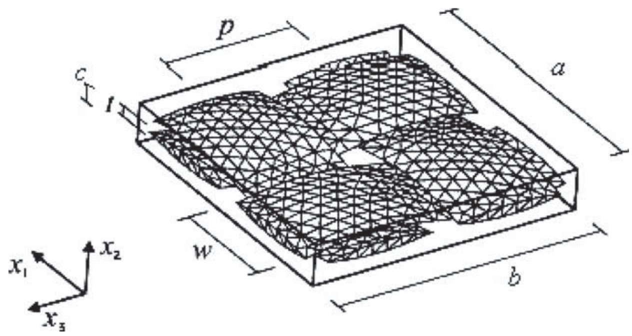

Figure 2.10: RUC of plain weave laminae made with solid elements [11]

Kueh and Pellegrino [26] applied a similar model approach to triaxial woven fabrics using one-dimensional beam elements, as shown in Figure 2.11. To ensure no relative motion at the interlacing points, crossover regions were constrained using multi-point constraints. The simulation results were validated against experimental data for the same material. The developed model accurately captured tensile, compressive, shear and bending stiffness within the linear geometric regime.

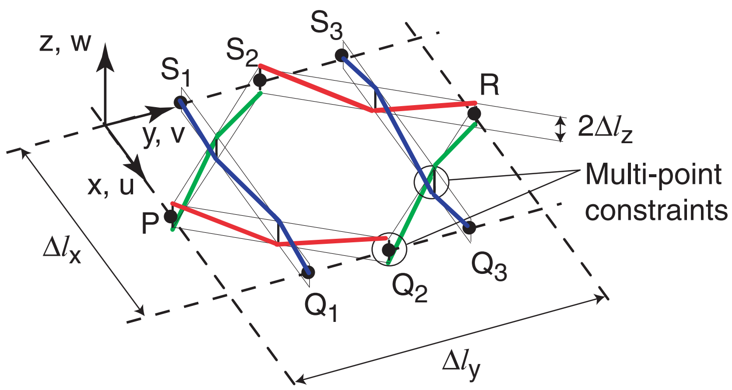

Figure 2.11: RUC of triaxial weave fabric with beam elements [26]

Mallikarachchi [17] extended this approach to model a two-ply plain weave composite laminate. The tow path was idealised using a fourth-root sine function to represent the weave geometry. To accurately capture the composite's behaviour, an adhesive layer was included between the tows. Additionally, a series of reference points, rather than a single one, was employed to connect the tow boundaries to the corresponding dummy nodes, as illustrated in Figure 2.12. This refinement prevents the formation of a rigid plate at the boundary face, which can occur when a single reference point is used. The stiffness values obtained from the model showed strong agreement with experimental data, validating its accuracy within the linear regime.

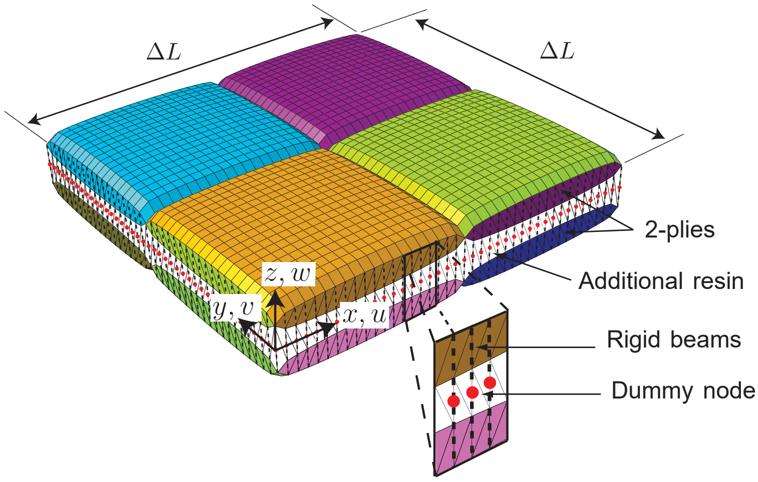

Figure 2.12: RUC of two-ply plain weave composite made with solid elements [17]

Yapa and Mallikarachchi [27] explored the mechanical behaviour of ultra-thin woven fibre composites under large deformations by extending Kirchhoff plate theory into the geometrically non-linear regime. In their model, tow cross-sections were idealised as equivalent rectangles and represented using two-node linear beam elements. Their study revealed that over-constraining at interaction regions could lead to non-convergence, emphasising the importance of incorporating realistic tow geometries and accurately simulating interaction properties to capture the true mechanical response of ultra-thin woven composites at high curvatures.

Wijesooriya et al. [28] developed an RUC using shell elements to model the tows and implemented cohesive behaviour at the interaction regions to provide a more realistic yet computationally efficient simulation. Additionally, a solid model incorporating both cohesive interactions and damage at contact regions was developed. This model successfully captured the reduction in bending moment up to a curvature of 0.05 mm^{-1}, highlighting the critical role of accurately modelling both cohesive and post-failure behaviour for reliable mechanical response predictions in thin woven composites.

Nadarajah et al. [29] extended this approach by developing a more realistic RUC model that captured the equivalent tow geometry and waviness using cubic Bézier splines. The geometry was generated using the commercially available TeX-GEN software and subsequently imported into Abaqus for simulation. The developed model successfully captured the initial bending stiffness of the composite, demonstrating the effectiveness of combining realistic geometry with advanced simulation tools for accurate mechanical behaviour prediction.

Chapter 3

Material Characterisation

This section presents the details of the two-ply plain weave carbon fibre material considered in this study. Geometric parameters were taken from the previous study done by Gamage [7] using XRCT analysis and basic constituent properties were obtained from the manufacturer's data sheets. The section also describes the idealisation procedure used to construct the representative unit cell for the two-ply plain-weave composite laminate, including both geometric idealisation and material homogenisation.

3.1 Geometric Properties

As illustrated in Figure 2.9, a plain-weave lamina may be identified as a repeating geometry. When two laminae are considered, however, the definition of RUC becomes considerably more challenging, as there are infinitely many possible configurations for stacking the plies. Soykasap [30] presented two extreme cases of such arrangements, referred to as fibre in-phase and fibre out-of-phase, as illustrated in Figure 3.1. These two cases are adopted in the present study as reference configurations.

Geometric parameters were taken from the previous study done by Gamage [7] using XRCT analysis, a non-invasive imaging method to study the internal morphology of objects covered by dense materials, as summarised in Table 3.1. Figure 3.2 shows an isometric view and a cross-sectional profile of the laminate obtained from XRCT imaging.

Table 3.1: Geometric properties of T300-1k/PMT-F4 epoxy laminate [7]

Nominal weave length, Δl (mm)	2.88
Average tow thickness, t_{tow} (mm)	0.06
Average tow width, w_{tow} (mm)	1.14
Average cross-sectional area of a tow, A_{tow} (mm^2)	0.0518

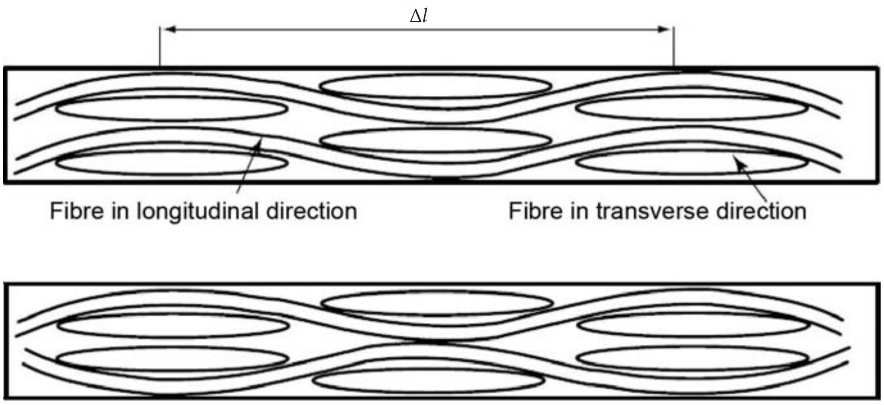

Figure 3.1: Fibre in-phase and fibre out-of-phase arrangements [30]

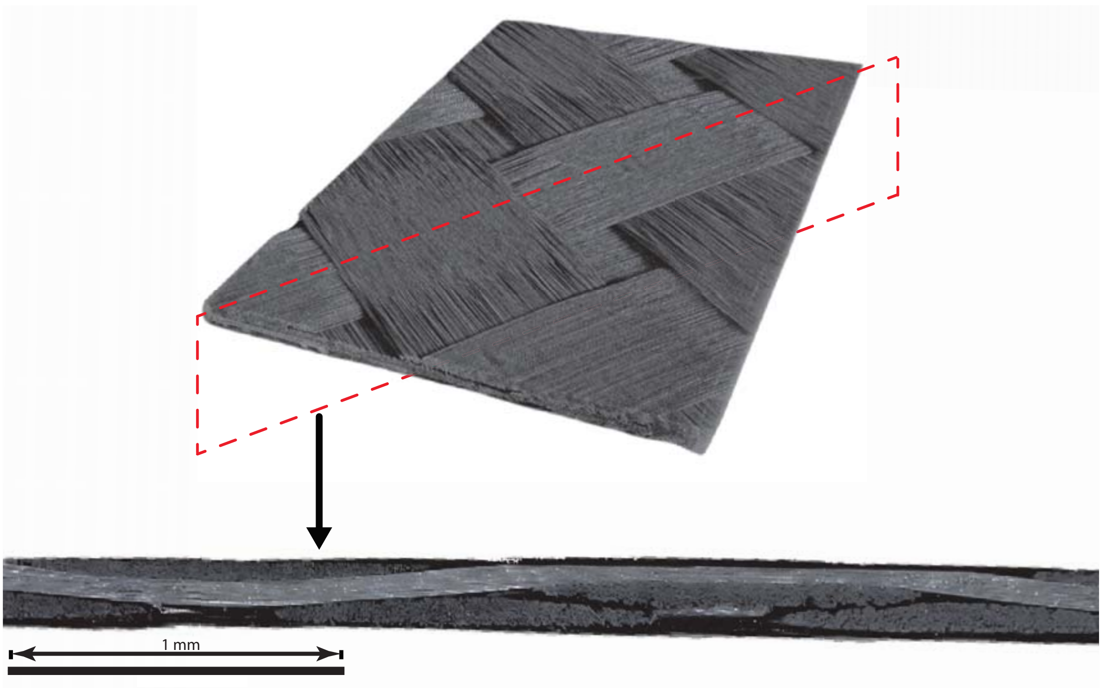

Figure 3.2: Micro-structure of two-ply plain weave T300/PMT-F4 laminate reconstructed by processing XRCT images [7]

3.2 Geometric Idealisation

To accurately represent the tow geometry observed in the XRCT scans, a cubic Bézier curve was fitted along the tow paths. The cubic Bézier spline used to describe the tortuous tow trajectories is defined in Equation 3.1.

$$B(k) = P_0(1-s)^3 + 3P_1 s(1-s)^2 + 3P_2 s^2(1-s) + P_3 s^3;\ 0 \leq s \leq 1 \tag{3.1}$$

where s is a non-dimensional parameter defining the position along the line and points P_0, P_1, P_2, and P_3 are specified according to the geometric characteristics of the tow under consideration.

Accurately incorporating the exact geometry of the tow cross-section into the model is not straightforward, as it varies along the length of the tow. To achieve a more realistic representation, the cross-section was idealised as a power ellipse that matches the tow width and thickness values reported in the literature. Parametric coordinates of the idealised tow cross-section are given by $C(k) = (C_x(k), C_y(k))$, where $k \in [0, 1]$. $C_x(k)$ and $C_y(k)$ are given by

$$C_x(k) = \frac{d}{2}\cos(2\pi k), \quad 0 \leq k \leq 1 \tag{3.2}$$

$$C_y(k) = \begin{cases} \frac{h}{2}(\sin(2\pi k))^n, & \text{if } 0 \leq k \leq 0.5 \\ -\frac{h}{2}(-\sin(2\pi k))^n, & \text{if } 0.5 < k \leq 1 \end{cases} \tag{3.3}$$

Here h, w, and n represent the minor diameter of the cross-section, major diameter of the cross-section, and shape exponent, respectively. For the cross-section considered, based on the tow width and thickness, a value of $n = 1.2$ was found to provide the best fit.

3.3 Material Properties

The composite examined in this study consists of T300-1k carbon fibre supplied by Torayca Incorporation [31] and PMT-F4 epoxy resin from PMT Prepreg Resin Systems [32]. The fibre and resin properties provided by the manufacturers are listed in Table 3.2. Properties not available in the datasheets were estimated from values reported in the literature [33, 34]. The fibre volume fraction, V_f, of the laminate was determined to be 0.62 by weighing five square specimens measuring 100 mm $\times$ 100 mm [7].

Table 3.2: Material properties of T300 fibres and PMT-F4 epoxy resin

Constituent Property	T300 Fibres [31]	PMT-F4 Resin [32]
Longitudinal modulus, E_1 (N/mm^2)	233,000	3,833
Transverse modulus, E_2 (N/mm^2)	23,100	3,833
Shear modulus, G_{12} (N/mm^2)	8,963	1,441
Poisson's ratio, ν_{12}	0.20	0.33
Density, ρ (kg/m^3)	1,760	1,210
Areal weight of fabric, W (g/m^2)	98	-

3.4 Homogenised Material Properties

Based on the constituent properties, the tows are idealised as a transversely isotropic material. The five independent engineering constants are determined as follows [35, 36]. In the calculations, the fibre volume fraction (V_f) is taken as 0.62, under the assumption that all the resin is contained within the tows.

The longitudinal extensional modulus and Poisson's ratio of the tows are estimated using the rule of mixtures.

$$E_1 \;=\; E_{1f}V_f + E_m(1 - V_f) \tag{3.4}$$

$$\upsilon_{12} \;=\; \upsilon_{13} \;=\; \upsilon_{12}V_f + \upsilon_m(1 - V_f) \tag{3.5}$$

However, using the rule of mixtures to estimate the transverse properties of a tow may produce inaccuracies due to differences in transverse strains and stresses between the fibre and resin. Consequently, the Halpin–Tsai semi-empirical relations are applied to calculate the transverse extensional modulus.

$$E_2 = E_3 = E_m \frac{1 + \chi\eta V_f}{1 - \eta V_f} \tag{3.6}$$

where,

$$\eta = \frac{E_{2f} - E_m}{E_{2f} - \chi E_m} \tag{3.7}$$

In this expression, the parameter χ quantifies the reinforcement of the composite and is taken as 2 [36].
The longitudinal shear modulus $G_{12} = G_{13}$ is also estimated using the Halpin-Tsai semi-empirical relations.

$$G_{12} = G_{13} = G_m \frac{(G_{12f} + G_m) + V_f(G_{12f} - G_m)}{(G_{12f} + G_m) - V_f(G_{12f} - G_m)} \tag{3.8}$$

Finally, transverse shear modulus, G_{23}, is determined by solving the quadratic equation presented by Quek et al. [37] and the transverse Poisson's ratio was calculated from Equation 3.9.

$$G_{23} = \frac{E_2}{2(1 + \upsilon_{23})} \tag{3.9}$$

The resulting values are summarised in Table 3.3.

Table 3.3: Estimated mechanical properties of cured T300-1k/PMT-F4 tow

Tow property	Value
Longitudinal extensional modulus, E_1 (N/mm^2)	145,920
Transverse extensional modulus, $E_2 = E_3$ (N/mm^2)	11,132
Longitudinal shear modulus, $G_{12} = G_{13}$ (N/mm^2)	3,782
Transverse shear modulus, G_{23} (N/mm^2)	3,680
Longitudinal Poisson's ratio, $\nu_{12} = \nu_{13}$	0.25
Transverse Poisson's ratio, ν_{23}	0.51

3.5 Finite Strain Non-linear Behaviour

Carbon fibre composite shells in bending fail at much higher strains [38, 39] and the material properties of carbon fibres have been reported to be highly non-linear at these large strains [40, 41, 42]. This non-linearity is primarily associated with tensile hardening and compressive softening of the fibres [43, 44]. Graphite crystallites exhibit high modulus in the plane of the graphite layers but significantly lower modulus in the transverse direction and in shear between layers. As the tensile load on a fibre increases, the crystallites tend to rotate and align more closely with the fibre axis, resulting in an increased fibre modulus, which is referred to as tensile hardening [38]. In contrast, the opposite effect occurs under compressive loading. Because of this, carbon fibres exhibit an increase in elastic modulus under tensile strains and a reduction in elastic modulus under compressive strains.

To represent this material non-linearity, some studies have utilised a constitutive model with linearly varying fibre elastic modulus, as described in Equation 3.10, which allows stress to be a quadratic function of strain in both tension and compression [45, 46].

$$E_f(\varepsilon) = E_{f,0}\,(1 + \gamma\varepsilon) \tag{3.10}$$

Here, $E_{f,0}$ denotes the fibre's elastic modulus at zero strain, while the coefficient γ represents the rate at which the modulus varies with strain. Although Equation 3.10 aligns reasonably well with experimental data for in-plane behaviour, a single γ value for both tension and compression is insufficient to capture bending non-linearity. Therefore, studies propose using distinct γ coefficients for tension and compression [47, 48], as shown in Equation 3.11.

$$E_f(\varepsilon) = \begin{cases} E_{f,0}(1+\gamma_c\varepsilon), & \varepsilon < 0 \\ E_{f,0}(1+\gamma_t\varepsilon), & \varepsilon \geq 0 \end{cases} \tag{3.11}$$

In addition, it is important to note that when composites with highly stretchable elastomeric resins are subjected to large strains, the material on the compression side experiences micro-buckling [39, 49]. In these systems, straight fibres embedded in the resin provide significant axial stiffness under tensile or small compressive loads. However, as the compressive loading increases, the fibres undergo micro-buckling, while the elastomeric resin accommodates large compressive deformations. Consequently, at higher strains, it becomes necessary to modify the model to allow the modulus to reduce to near zero at a critical compressive strain, as described in Equation 3.12 [49].

$$E_f(\varepsilon) = \begin{cases} E_{f,b}, & \varepsilon < \varepsilon_{cr} \\ E_{f,0}(1+\gamma_c\varepsilon), & \varepsilon_{cr} < \varepsilon < 0 \\ E_{f,0}(1+\gamma_t\varepsilon), & \varepsilon \geq 0 \end{cases} \tag{3.12}$$

Here, $E_{f,b}$ denotes the reduced modulus of carbon fibres once the compressive strain exceeds a critical value ε_{cr}. The critical strain value was taken as 0.016 from the compressive response of the laminate [47], and the minimum modulus was considered to be the transverse modulus of the tow. Equation 3.13 was formulated to represent the constitutive model for a homogenised tow. Initial fibre modulus values presented in Table 3.3 together with coefficients γ_c and γ_t for T300 fibres were set to 14 and 6 based on Keryvin et al. [47], respectively. A higher coefficient in compression implies that the compressive softening effect predominates over tension stiffening at higher curvatures, and because of this, a shift in the neutral axis position was also observed at higher curvatures [47, 50]. Although in linear bending the tensile and compressive strains would be equal in magnitude, the compressive strains can be 25% higher than the tensile strain under high curvatures for thin composite laminates [51].

$$E_{tow}(\varepsilon) = V_f \left\{ \begin{array}{ll} E_{f,b}, & \varepsilon < \varepsilon_{cr} \\ E_{f,0}(1+\gamma_c\varepsilon), & \varepsilon_{cr} < \varepsilon < 0 \\ E_{f,0}(1+\gamma_t\varepsilon), & \varepsilon \geq 0 \end{array} \right\} + (1-V_f)\ E_{\text{resin}}(\varepsilon) \tag{3.13}$$

Chapter 4

Multi-Scale Numerical Modelling

This section presents the proposed multi-scale model to capture the observed non-linear bending behaviour. Multi-scale modelling technique has been utilised to predict macroscopic properties of the composite by linking the underlying micro-structure through volume averaging of field variables, conserving consistency. The necessity of multi-scale modelling arises from the inherently complex nature of micro-scale architecture, which demands high computational resources and yields excessive irrelevant information when all details are included in a single model.

4.1 Geometric Modelling of Tows

Two distinct approaches were employed in this study: one assuming a tow-only architecture and the other incorporating the resin in between two plies. The aim of using these two approaches was to assess the effectiveness of resin in accurately simulating contact behaviour at the interfacial regions. To evaluate the influence of material non-linearity on the observed reduction in bending stiffness, both linear and non-linear material analyses were conducted for the tow-only and resin-embedded models within the geometrically non-linear regime.

An RUC was established for the two-ply woven composite to capture key meso-mechanical features such as the weave pattern, tow cross-section, and ply stacking sequence, that govern the macroscopic kinematic behaviour. The geometry of the RUC was informed by detailed 3D volumetric data obtained via XRCT, as described in Section 3.1. Tow geometries for both fibre in-phase and out-of-phase configurations were generated using the TexGen finite element pre-processor, as illustrated in Figure 4.1. The input parameters used in the TexGen weave module are listed in Table 3.1. RUC configuration was chosen based on the size sensitivity analysis conducted by Gowrikanthan et al.[52], striking a balance between computational efficiency and the retention of essential meso-structural features that influence the global response.

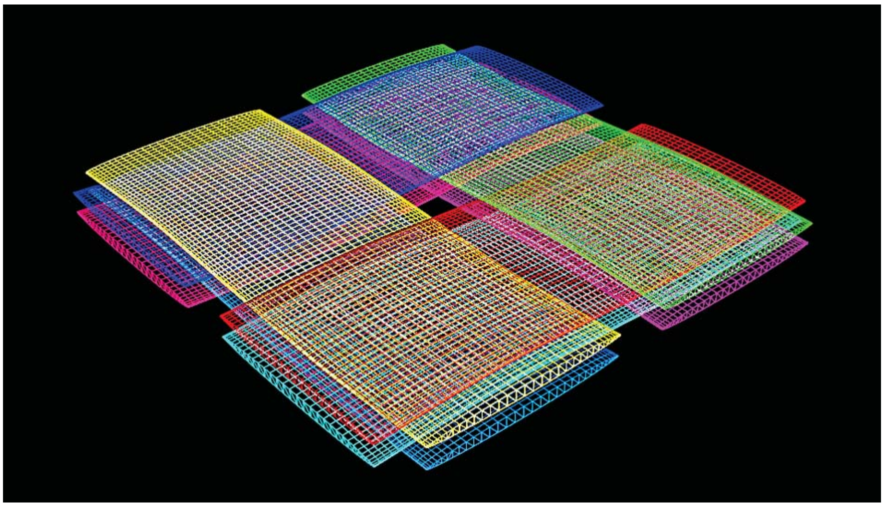

Figure 4.1: Tow geometry modelled in TexGen finite element pre-processor for fibre-in-phase arrangement

Each tow was discretised using the TexGen finite element pre-processor, employing a combination of eight-node linear brick elements with reduced integration (`C3D8R`) and six-node linear triangular prism elements (`C3D6`). Four element layers were included through the thickness to enhance accuracy and prevent hourglassing. Fewer layers would result in only one or two integration points through the thickness, owing to the reduced integration scheme, which would limit the accurate representation of deformations, particularly under bending.

A circumferential mesh density of 70 nodes and an along-tow density of 90 nodes was adopted, consistent with the mesh sensitivity analyses reported by Gowrikanthan et al. [52]. The resulting input file (**.inp*) was imported into Abaqus/Standard as an orphan mesh for mechanical simulations. The homogenised material properties calculated in Section 3.4 were assigned to each tow, taking into account the corresponding material orientations.

4.2 Modelling of Resin

To represent a more realistic RUC, a resin pocket was introduced in the gap between the upper and lower plies. The resin was embedded following the same tow geometries developed for the in-phase and out-of-phase configurations. The resin pocket was included only in the region between the two plies, as the experimental specimens were fabricated with a predetermined resin volume sufficient only to fill this gap.

To construct the resin pocket geometry, the surface of the tow-only model was first exported as a **.sat* file using the `Plug-ins` → `Create geometry from mesh` option in Abaqus. The exported **.sat* file, containing eight surface bodies, was then imported into SolidWorks. Using the `Tools` → `Thicken` function, the surface bodies were converted into solid bodies and saved as a **.step* file. Subsequently, the tow volume was subtracted from a 2.88 mm × 2.88 mm × 0.12 mm solid body using the `Insert` → `Features` → `Combine` option to obtain the resin volume between plies. Regions where the two plies come into contact, being infinitesimally thin, were removed using the same `Combine` command to prevent numerical errors. Additionally, areas without tows were removed, as shown in Figure 4.2, since resin cannot remain in these locations during high-pressure impregnation in the manufacturing process.

Figure 4.2: Geometry of resin layer modelled in SolidWorks

4.3 Boundary Conditions

Boundary conditions were applied during the homogenisation procedure to more accurately capture the representative behaviour of the material and the associated size effects of the continuum.

In first-order computational homogenisation, each node in the RUC is described by two position vectors: X, the position in the reference (undeformed) configuration, and x, the position in the current (deformed) configuration. The displacement vector is then defined in the standard way:

$$u(X) = x(X) - X. \tag{4.1}$$

The micro-scale displacement at a node is decomposed into a uniform macro-scale contribution and a micro-scale fluctuation term:

$$u_m(X_M) = F_M X_M + w_m(X_M) \tag{4.2}$$

where F_M is the macro-scale deformation gradient and w_m is the micro-fluctuation displacement. Substituting the above definitions gives:

$$w_m(X_M) = u_m(X_M) - F_M X_M = x_m(X_M) - X_M - F_M X_M \tag{4.3}$$

RUC modelling require the fluctuation field to be identical on opposite faces:

$$w_m^+ = w_m^- \tag{4.4}$$

where, the superscripts "+" and "–" indicate quantities taken in opposite faces. For instance, "+" denotes a point located on the right or upper face, whereas "–" designates a point on the left or lower face. Using the decomposition $u_m = x_m - X_M$ and rearranging, this condition becomes:

$$x_m^+ - x_m^- = F_M \left(X_M^+ - X_M^- \right) \tag{4.5}$$

which states that the difference in the deformed positions of opposite nodes is dictated by the macro-scale deformation gradient applied to the difference in their reference positions. Finally, the condition

$$n_m^+ = n_m^-, \tag{4.6}$$

ensures that opposite faces possess matching outward normals, which guarantees consistent pairing of nodes on opposite RUC boundaries. This geometric requirement does not introduce additional algebraic constraints in the finite element model.

Adhering to the general forms, the procedure suggested by Mallikarachchi [17, 53] was enforced in the meso-scale model using following equation constraints applied on the reference nodes and dummy nodes.

$$\begin{aligned}
\text{In-plane displacements:}\quad & \Delta u^x = \varepsilon_x \Delta L, && \Delta v^x = \tfrac{1}{2}\gamma_{xy}\Delta L,\\
& \Delta u^y = \tfrac{1}{2}\gamma_{xy}\Delta L, && \Delta v^y = \varepsilon_y \Delta L,\\
\text{Out-of-plane displacements:}\quad & \Delta w^x = -\tfrac{1}{2}\kappa_{xy} y \Delta L, && \Delta w^y = -\tfrac{1}{2}\kappa_{xy} x \Delta L,\\
\text{Rotations:}\quad & \Delta\theta_x^x = -\tfrac{1}{2}\kappa_{xy}\Delta L, && \Delta\theta_y^x = \kappa_x \Delta L,\\
& \Delta\theta_x^y = -\kappa_y \Delta L, && \Delta\theta_y^y = \tfrac{1}{2}\kappa_{xy}\Delta L,\\
& \Delta\theta_z^x = 0, && \Delta\theta_z^y = 0
\end{aligned} \tag{4.7}$$

Here, θ denotes the rotations; the subscripts indicate the directions of deformation, while the superscripts specify the directions of the corresponding pair of boundary nodes, which share the same x or y coordinates.

Mesh element nodes at the boundaries of the tows in the upper and lower plies were selected using a Python script in Abaqus Macros and connected to the corresponding reference nodes. To directly transfer applied strains to the tows, all degrees of freedom between the reference nodes and boundary nodes were rigidly coupled using MPC beam connectors. Reference nodes were defined for each pair of boundary nodes of adjacent tows in different plies. A dummy node was introduced to establish a connection between reference nodes by applying `Equation` constraints in Abaqus/Standard for every matched pair of reference nodes located on opposite sides of the RUC, as illustrated in Figure 4.3. All reference and dummy nodes were positioned in the neutral plane of the RUC to prevent the introduction of additional moments due to eccentricities.

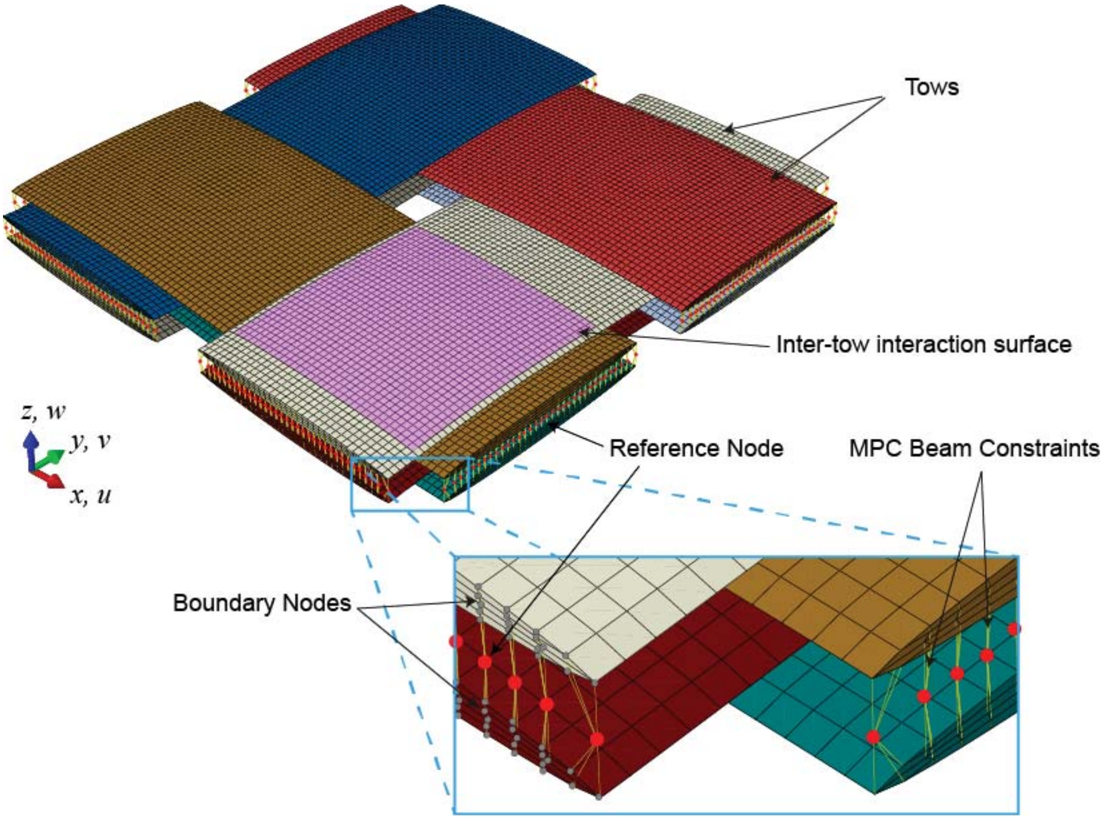

Figure 4.3: Finite element model of RUC model

4.4 Tow–Tow Interaction

Woven composites undergoing large curvatures may experience inter-tow micro-slipping and delamination, particularly in ultra-thin configurations. Accurate modelling of these effects is essential, given the hypothesised role of tow slipping in the observed bending stiffness degradation.

Abaqus/Standard provides two approaches for cohesive interactions: surface-based cohesion and cohesive elements. Due to the thin interaction zones and complex geometry, surface-based cohesive contact with traction separation behaviour was preferred. For tow only models, a total of 12 contact regions were defined, eight intra ply and four inter ply, using manually selected surfaces from the orphan mesh. In contrast, a total of 20 contact regions were defined for resin-embedded models, as shown in Figure 4.4.

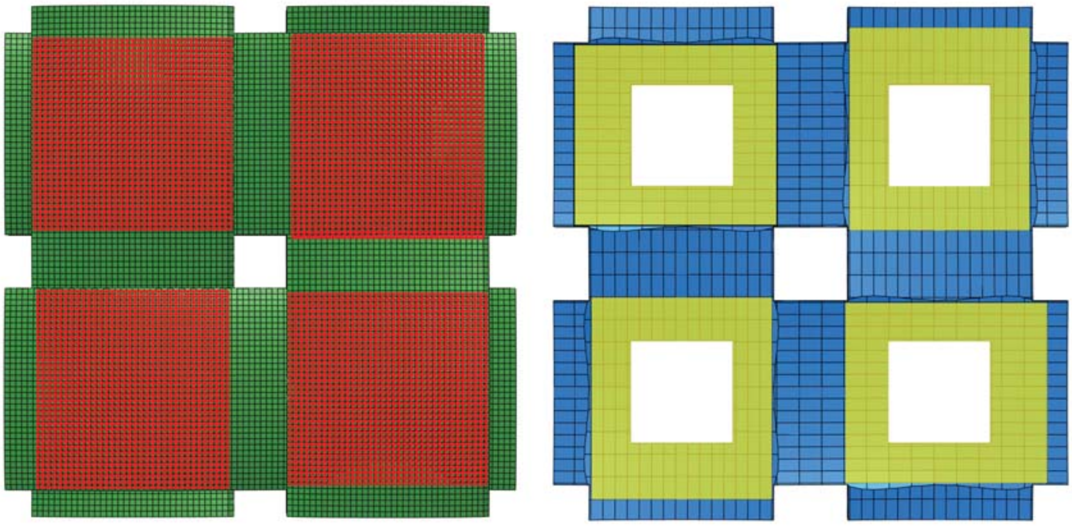

Figure 4.4: Manually selected contact areas for the tows and resin

The cohesive behaviour is defined via a bilinear traction–separation law:

$$\begin{bmatrix} t_n \\ t_s \\ t_t \end{bmatrix} = \begin{bmatrix} K_{nn} & 0 & 0 \\ 0 & K_{ss} & 0 \\ 0 & 0 & K_{tt} \end{bmatrix} \begin{bmatrix} \delta'_n \\ \delta'_s \\ \delta'_t \end{bmatrix} \tag{4.8}$$

where $t_{(..)}$ and $\delta'_{(..)}$ denote traction stresses and traction separations corresponding to normal, sliding and tearing modes denoted by subscripts n, s and t, respectively. Note that uncoupled behaviour is assumed between modes. The cohesive stiffness parameters are derived by simulating a PMT-F4 resin block using XFEM as elastic properties depend on underlying element stiffness.

From the resulting traction–separation curves, the coefficients were estimated to be $K_{nn} = 253{,}722$ MPa/mm and $K_{ss} = K_{tt} = 90{,}561$ MPa/mm [28].

Damage initiation was modelled using a maximum nominal stress criterion. For inter-ply contact, the peak contact stresses were determined to be 17.6 MPa in the normal direction and 6.3 MPa in the transverse shear directions, based on the inter-laminar fracture toughness of non-woven T300 carbon fibre/epoxy composites fabricated from unidirectional prepreg tapes [54, 55]. Intra-ply contact was assumed to be twice as strong, in agreement with previously reported values for woven fibre composites [56, 57].

4.5 Formation of Constitutive Relationship

The effective macroscopic behaviour of the composite is expressed through the ABD stiffness matrix, which relates mid-plane strains and curvatures to membrane forces and bending moments [11, 26, 58]. Although the microstructure of woven composites is heterogeneous, the laminate is sufficiently thin at the macroscopic scale for transverse shear effects to be neglected. At the meso-scale, the woven pattern may induce local warping due to stiffness mismatches and tow waviness. However, for thin laminates, the characteristic wavelength of global bending is considerably larger than the dimensions of a single weave unit cell, so these local variations are effectively smoothed out through homogenisation. As a result, the representative unit cell is modelled as a thin shell according to the Kirchhoff–Love hypothesis. The plane-section assumption is therefore considered valid at the homogenised scale employed in this study, even though it is not strictly applicable at the microscopic level.

The in-plane displacements are approximated using first-order Taylor expansions, while the out-of-plane displacement is represented using a second-order expansion:

$$u = u_0 + \varepsilon_x \, x + \frac{1}{2}\varepsilon_{xy} \, y \tag{4.9}$$

$$v = v_0 + \varepsilon_y \, y + \frac{1}{2}\varepsilon_{xy} \, x \tag{4.10}$$

$$w = w_0 + \left(\frac{\partial w}{\partial x}\right)_0 x + \left(\frac{\partial w}{\partial y}\right)_0 y + \frac{1}{2}\left(\frac{\partial^2 w}{\partial^2 x}\right)_0 x^2 + \frac{1}{2}\left(\frac{\partial^2 w}{\partial^2 y}\right)_0 y^2 + \left(\frac{\partial^2 w}{\partial x \partial y}\right)_0 xy \tag{4.11}$$

The kinematic variables for the representative unit cell (RUC) are defined as follows:

$$\varepsilon_x = \frac{\partial u}{\partial x} \tag{4.12}$$

$$\varepsilon_y = \frac{\partial v}{\partial y} \tag{4.13}$$

$$\gamma_{xy} = \frac{\partial u}{\partial y} + \frac{\partial v}{\partial x} \tag{4.14}$$

$$\kappa_x = -\frac{\partial^2 w}{\partial x^2} \tag{4.15}$$

$$\kappa_y = -\frac{\partial^2 w}{\partial y^2} \tag{4.16}$$

$$\kappa_{xy} = -2\frac{\partial^2 w}{\partial x\, \partial y} \tag{4.17}$$

Here, x and y denote the two in-plane principal directions, while u, v, and w represent the displacements in the x, y, and z directions, respectively. It should be noted that the engineering shear strain and twice the surface twist are employed to define the shear strain and twisting curvature, respectively, in accordance with the classical theory of laminated plates.
The resulting constitutive relation is:

$$\begin{Bmatrix} N_x \\ N_y \\ N_{xy} \\ -- \\ M_x \\ M_y \\ M_{xy} \end{Bmatrix} = \begin{pmatrix} A_{11} & A_{12} & A_{16} & | & B_{11} & B_{12} & B_{16} \\ A_{21} & A_{22} & A_{26} & | & B_{21} & B_{22} & B_{26} \\ A_{61} & A_{62} & A_{66} & | & B_{61} & B_{62} & B_{66} \\ -- & -- & -- & -- & -- & -- & -- \\ B_{11} & B_{21} & B_{61} & | & D_{11} & D_{12} & D_{16} \\ B_{12} & B_{22} & B_{62} & | & D_{21} & D_{22} & D_{26} \\ B_{16} & B_{26} & B_{66} & | & D_{61} & D_{62} & D_{66} \end{pmatrix} \begin{Bmatrix} \varepsilon_x \\ \varepsilon_y \\ \gamma_{xy} \\ -- \\ \kappa_x \\ \kappa_y \\ \kappa_{xy} \end{Bmatrix}. \tag{4.18}$$

In a concise form,

$$\begin{Bmatrix} N \\ M \end{Bmatrix} = \begin{pmatrix} A & B \\ B & D \end{pmatrix} \begin{Bmatrix} \varepsilon \\ \kappa \end{Bmatrix} \tag{4.19}$$

where N and M are in-plane forces and moments per unit width, and ε and κ are mid-plane strains and curvatures. The sub-matrices $[A]$, $[B]$, and $[D]$ denote extensional, coupling and bending stiffnesses, respectively. As the study focuses on bending behaviour, the $[D]$ sub-matrix is of particular interest.

Six independent simulations are performed on the RUC, each with a unit deformation applied to one kinematic variable, while the others are constrained to zero (i.e, when $\varepsilon_x = 1$, $\varepsilon_y = \varepsilon_{xy} = \kappa_x = \kappa_y = \kappa_{xy} = 0$) as illustrated in Figure 4.5.

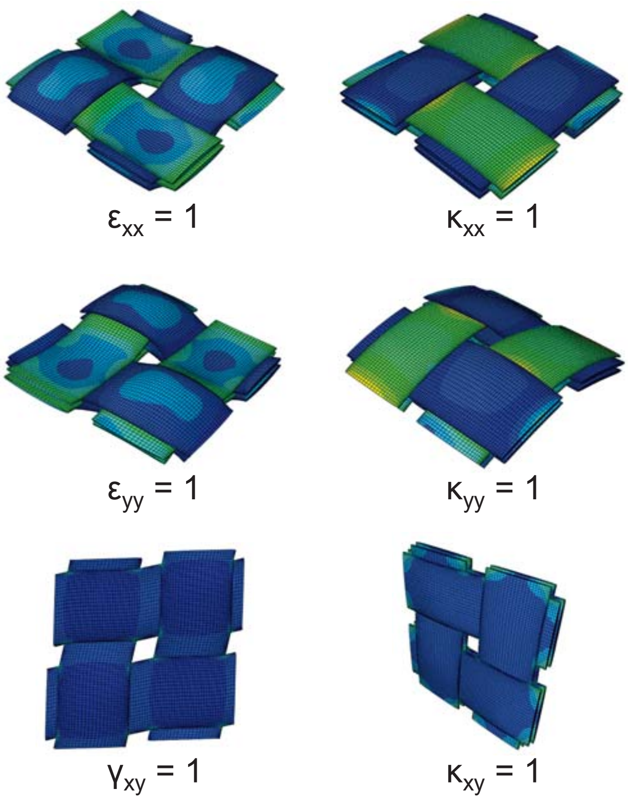

Figure 4.5: Deformed configurations for analyses performed in geometrically linear region

All strains and curvatures were applied to the model via prescribed dummy nodes. The displacements and rotations of each dummy node, along with the corresponding forces and moments at the reference nodes, were obtained by directly editing the Abaqus **.inp* file. All output data were extracted from the Abaqus **.dat* file, and a MATLAB script was used to read and post-process these results to assemble the ABD matrix. Using the extracted boundary forces, moments, and displacements, the ABD matrix was constructed according to the principle of virtual work:

$$N_{xx}\varepsilon_{xx}\Delta l_x\Delta l_y = \sum\left(F_xu + F_yv + F_zw + M_x\theta_x + M_y\theta_y + M_z\theta_z\right) \tag{4.20}$$

Here, F and M represent the boundary force and moment vectors, while u, v, w, θ_x, θ_y, and θ_z denote the nodal displacements and rotations. The quantities Δl_x and Δl_y correspond to the dimensions of the RUC in the x and y directions, respectively. Contributions from all 272 reference nodes (connected to 2,656 boundary nodes) are summed to obtain the homogenised stiffness matrix:

$$ABD = \frac{U^T F}{\Delta l_x \cdot \Delta l_y} \tag{4.21}$$

where U and F are the full nodal displacement and force matrices of size of 1632×6 (corresponding to total number of degrees of freedom of reference nodes ($272 \times 6 = 1632$) and six deformation quantities).

4.6 Non-linear Analyses

Non-linear analyses were performed up to a maximum curvature of 0.2 mm^{-1}, and geometric non-linearity was addressed by extracting force and deformation quantities incrementally, as shown in Figure 4.6. All outputs from the geometrically non-linear analysis were extracted from the Abaqus **.dat* file at equal time intervals to plot the bending moment per unit width against the applied curvature using a Python script developed for this purpose. The applied curvature at each time step was calculated by linearly interpolating between consecutive time intervals, as the curvature was applied in a linear manner.

To capture the complex material behaviour described in Chapter 3.5, a User Defined Field (USDFLD) subroutine was employed to model the material response in accordance with Equation 3.13. This subroutine enables field variable values to be assigned directly at element integration points as functions of element quantities, such as stress or strain. Material-modifying subroutines are typically called at the start of each iteration. During the first call, the initial stiffness matrix is generated based on the configuration at the beginning of the increment. In the second call, the stiffness matrix is updated according to the new configuration. For all subsequent iterations, the subroutine is executed once per iteration, with the configuration evaluated using the stiffness matrix obtained at the end of the preceding iteration, as illustrated in Figure 4.7.

The USDFLD subroutine is capable of accessing solution data at the end of each increment, allowing material properties to be defined as functions of these results, such as stress (σ) and strain (ε). In this study, field variable values at the current material points were interpolated from nodal values at the end of each increment and used to update material properties that depend on the field variables. The functional relationship can be specified either via tabular input or through additional subroutines. In particular, the longitudinal extensional modulus of the tows (E_{11}) was defined as a function of axial strain in tabular form over the range $[-0.025, 0.025]$ with increments of 0.001. This strain range was determined from a preliminary simulation conducted at the same curvature

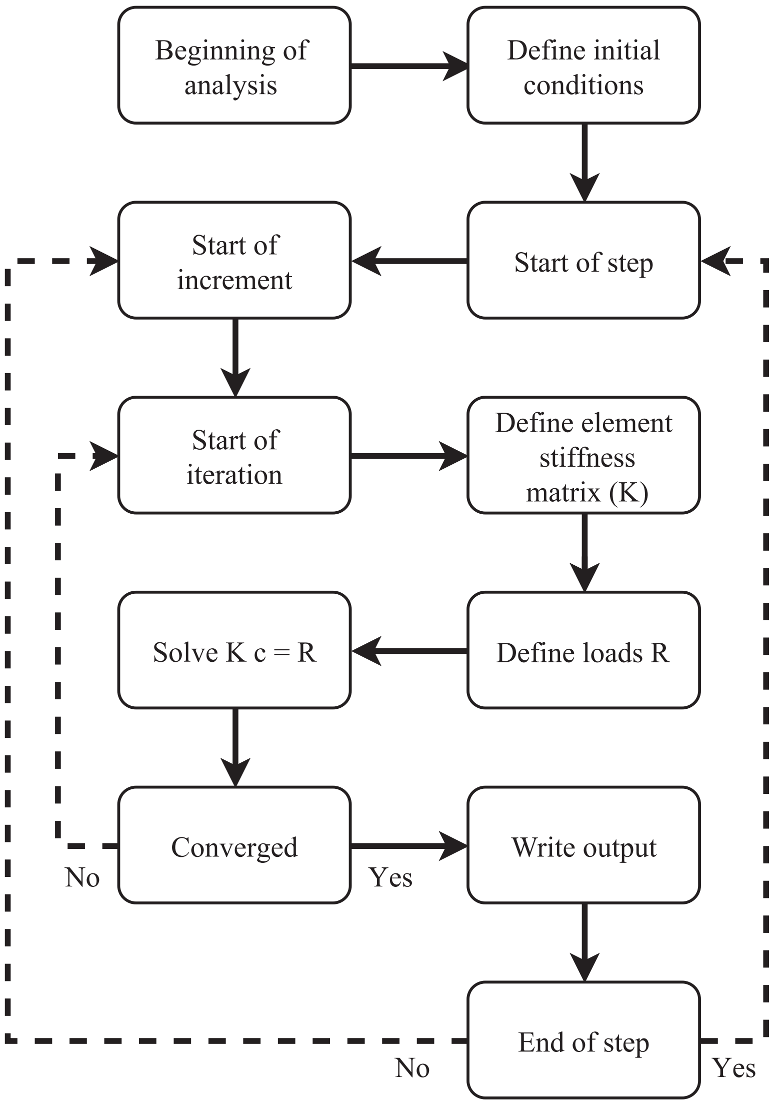

Figure 4.6: Global flow in ABAQUS

without material non-linearity, which identified the maximum tensile and compressive strains. Abaqus performs linear interpolation between tabular points and adopts the nearest available value if the field variable exceeds the specified range, without performing extrapolation.

Since the USDFLD subroutine accesses material point quantities only at the start of each increment, the solution dependence within the increment is explicit; that is, material properties for a given increment are not affected by calculations performed during that increment. Abaqus's automatic time incrementation algorithm reduces the increment size when convergence is

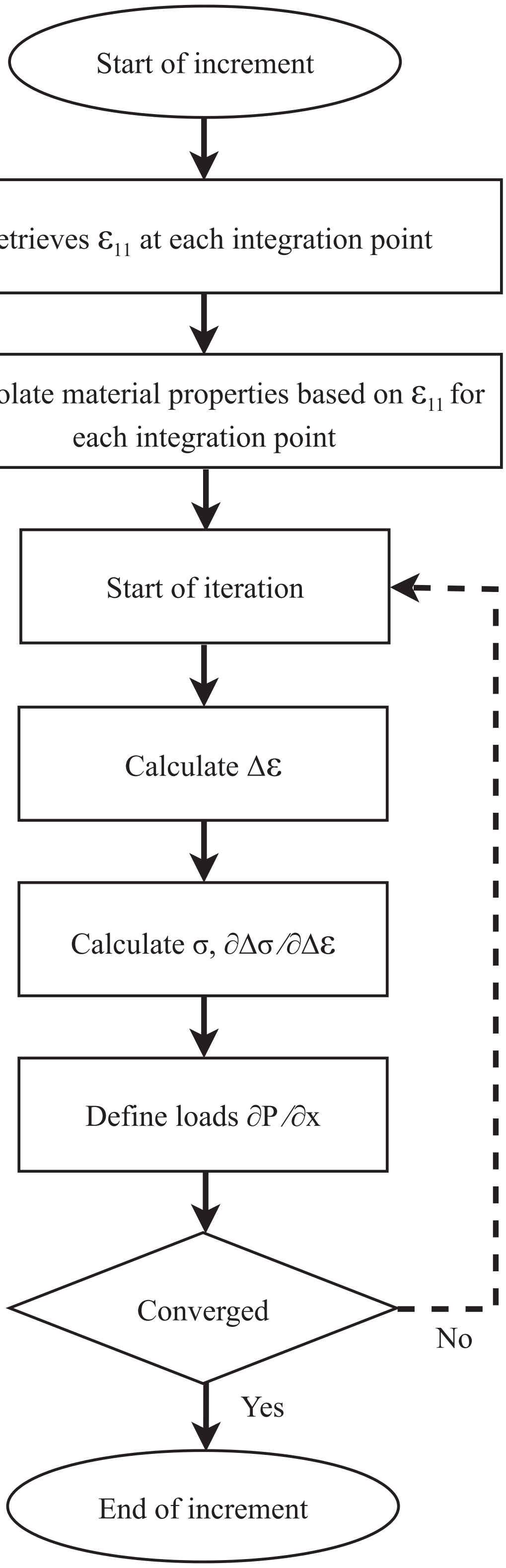

Figure 4.7: Flowchart of USDFLD subroutine within a time increment

challenging. Upon completion of the simulation, as in linear analysis, the displacements and rotations of dummy nodes, along with the forces and moments at reference nodes, were extracted at the end of each increment via node output requests.

Chapter 5

Results and Discussion

In this study, both geometrically and materially linear analyses were first conducted, and the resulting ABD matrices for the fibre in-phase and fibre out-of-phase configurations were compared. Subsequently, non-linear analyses were performed, incorporating geometric non-linearity, material non-linearity, and cohesive failure. The numerical results obtained from these simulations were validated against the experimental data reported by Gamage [7].

5.1 Comparison of the ABD Stiffness Matrices of In-Phase and Out-of-Phase Models

Geometrical and material linear analyses were conducted for both fibre in-phase and fibre out-of-phase configurations across all six deformation modes described in Section 4.5. The resulting ABD matrix for fibre in-phase arrangement is presented below.

$$ABD_{In-phase} = \begin{pmatrix} 9,561 & 1,039 & 0 & | & 0 & 0 & 0 \\ 1,039 & 9,561 & 0 & | & 0 & 0 & 0 \\ 0 & 0 & 384 & | & 0 & 0 & 0 \\ -- & -- & -- & -- & -- & -- & -- \\ 0 & 0 & 0 & | & 39.9 & 1.2 & 0 \\ 0 & 0 & 0 & | & 1.2 & 39.9 & 0 \\ 0 & 0 & 0 & | & 0 & 0 & 2.1 \end{pmatrix} \tag{5.1}$$

The results indicate that there is no coupling between the extensional and bending stiffnesses. The initial bending stiffness obtained from the CBT experiments 39.76 $\pm$ 3.92 Nmm [7] is in close agreement with the D_{11} value obtained from the analysis.

Presented below is the ABD stiffness matrix for fibre out-of-phase configuration.

$$ABD_{Out-of-phase} = \begin{pmatrix} 10,257 & 362 & 0 & | & 0 & 0 & 0 \\ 362 & 10,257 & 0 & | & 0 & 0 & 0 \\ 0 & 0 & 382 & | & 0 & 0 & 0 \\ -- & -- & -- & -- & -- & -- & -- \\ 0 & 0 & 0 & | & 36.1 & 5.2 & 0 \\ 0 & 0 & 0 & | & 5.2 & 36.1 & 0 \\ 0 & 0 & 0 & | & 0 & 0 & 2.1 \end{pmatrix} \quad (5.2)$$

For this configuration also, there is no coupling between the extensional and bending stiffnesses. In the extensional stiffness matrix, the fibre out-of-phase arrangement exhibits a higher A_{11} and a lower A_{12} compared with the fibre in-phase configuration. In contrast, in the bending stiffness matrix, the fibre out-of-phase arrangement shows a lower D_{11} and a higher D_{12} value than the fibre in-phase configuration. However, it is important to note that for both arrangements the cross-sectional areas under tensile loading are identical, and the second moments of area under bending are also the same, as illustrated in Figure 5.1.

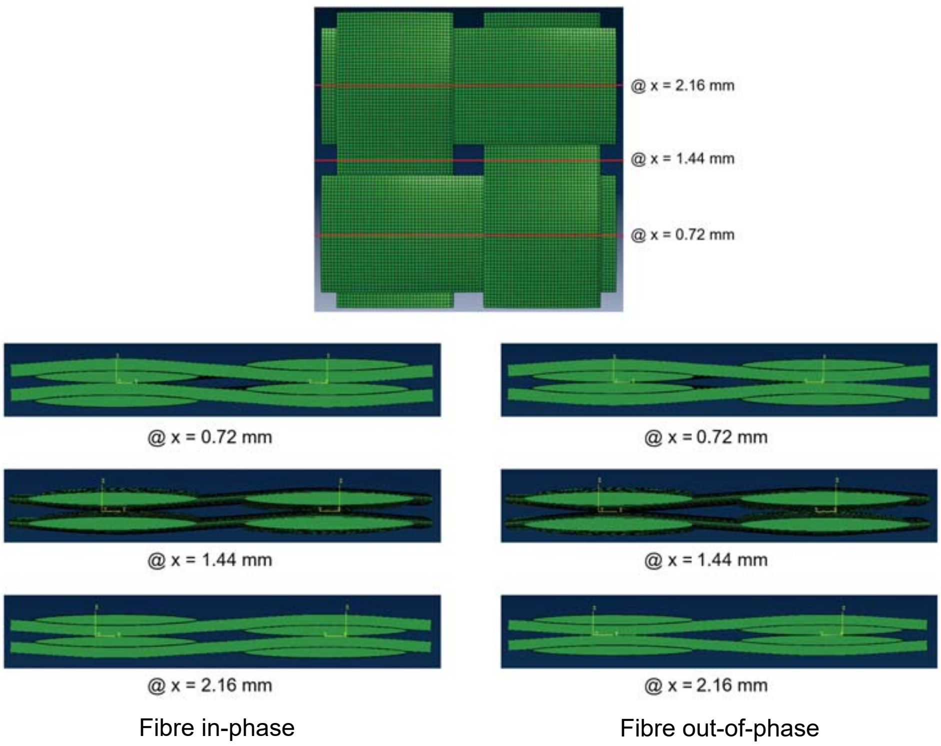

Figure 5.1: Cross-sections at different locations for fibre in-phase and out-of-phase configurations

These variations can be explained by considering meso-scale tow kinematics. The application of the same axial tensile force to both configurations is illustrated in Figure 5.12. In this figure, the green arrows represent the applied external forces, the red arrows denote the internal tensile stresses, and the black arrows indicate the directions of tow movement. In the fibre in-phase configuration, the tows tend to straighten in the same z-direction under tensile loading. As a result, the constraint imposed by the transverse tows is reduced, allowing the fibres to deform cooperatively.

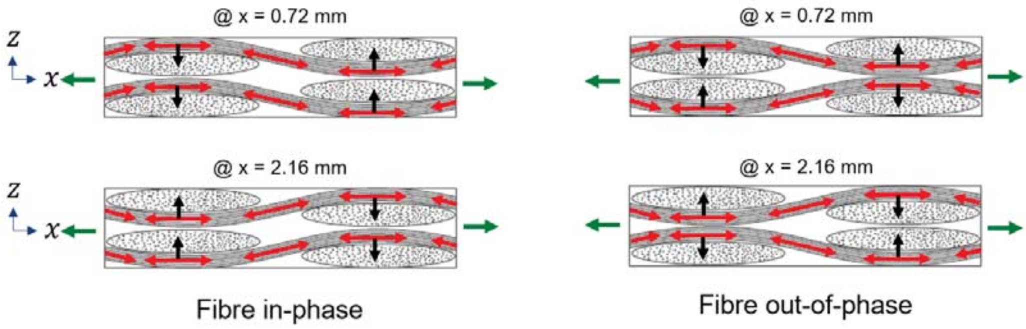

Figure 5.2: Meso-scale tow movements under tensile loading

In contrast, for the fibre out-of-phase configuration, the tows straighten in opposite z-directions. This opposing deformation increases the constraint imposed by the transverse tows, and the out-of-plane motions of the fibres partially cancel each other. Consequently, for an applied tensile load of the same magnitude, the fibre out-of-phase configuration exhibits a lower axial strain ε_1, as the reduction in tow waviness is less pronounced compared to the in-phase configuration. This leads to a higher effective extensional stiffness, and hence a larger A_{11} value for the fibre out-of-phase arrangement.

The coefficient A_{12} quantifies the coupling between axial and transverse deformations. In the fibre in-phase arrangement, the transverse tows require a larger lateral rearrangement as they move together in opposite directions, from $x = 0.72$ mm to $x = 2.16$ mm. By contrast, the fibre out-of-phase arrangement requires less lateral rearrangement. Consequently, the fibre in-phase configuration exhibits a larger transverse strain, ε_2, compared with the out-of-phase configuration, resulting in a higher A_{12} value for the in-phase arrangement.

The coefficient A_{66} characterises the in-plane shear stiffness of the laminate. Assuming that the intra-ply interactions are similar for both configurations, comparable A_{66} values are expected for the fibre in-phase and fibre out-of-phase arrangements. This expectation is confirmed by the numerical results, which show that the computed A_{66} values for the two configurations are nearly identical.

Now, consider the application of the same bending moment to both configurations, as illustrated in Figure 5.3. In this figure, the green arrows represent the applied external bending moment, the red arrows denote the internal tensile stresses, the blue arrows indicate the internal compressive stresses, and the black arrows show the directions of tow movement. Under the applied bending moment, the tows in tension tend to reduce their waviness, whereas the tows in compression tend to increase their waviness.

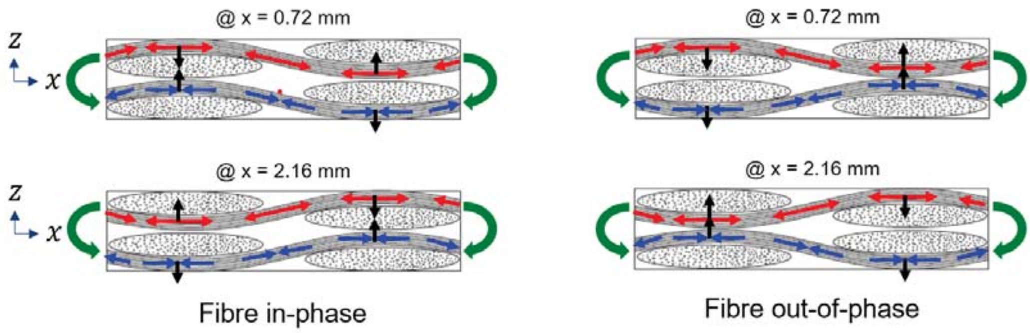

Figure 5.3: Meso-scale tow movements under bending

In the fibre in-phase configuration, the resulting z-displacements in the plies are opposite, leading to greater resistance from the transverse fibres. In contrast, for the fibre out-of-phase configuration, the resulting z-displacements are compatible, resulting in less resistance from the transverse fibres. Consequently, for an applied bending moment of the same magnitude, the fibre in-phase configuration exhibits a lower longitudinal curvature, κ_1, which corresponds to a higher effective bending stiffness and, hence, a larger D_{11} value.

Furthermore, in the fibre in-phase arrangement, a larger proportion of the deformation is accommodated by axial strain, whereas in the fibre out-of-phase configuration, more deformation is accommodated by shear. As a result, the longitudinal stress per unit curvature is higher in the fibre in-phase arrangement. Figure 5.4 compares the longitudinal stresses at a curvature of 0.2 mm^{-1} for both configurations.

For the fibre out-of-phase configuration, the transverse tows require a larger lateral rearrangement as they move together in opposite directions, from $x = 0.72$ mm to $x = 2.16$ mm. By contrast, the fibre in-phase arrangement requires less lateral rearrangement. This difference in tow kinematics results in

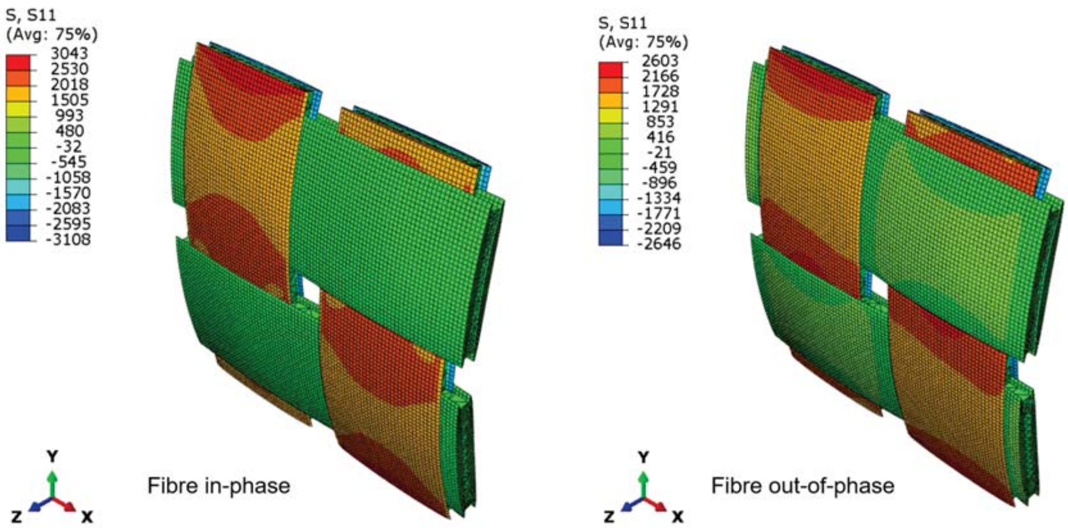

Figure 5.4: Longitudinal stress at 0.2 mm^{-1} curvature

a higher D_{12} value for the out-of-phase arrangement.

The coefficient D_{66} is also found to be nearly identical for both fibre in-phase and fibre out-of-phase arrangements. This parameter represents the laminate resistance to twisting curvature and is primarily governed by the in-plane shear stiffness of the tows and the overall thickness distribution of the laminate. As both configurations share identical material properties, laminate thickness, and weave architecture, the mechanisms controlling shear deformation under twisting are effectively the same. Consequently, the meso-scale tow kinematics associated with twisting are largely insensitive to the relative phase arrangement of the fibres, resulting in identical D_{66} values for both configurations.

5.2 Moment-Curvature Response of In-Phase Tow-only Models

Figure 2.7 shows that the bending stiffness of the two-ply plain-weave laminate decreases progressively with increasing curvature. This behaviour is consistent with the observations of Mallikarachchi and Pellegrino [6], who reported comparable stiffness reductions in similar composite specimens at higher curvatures. In their study, the bending moment decreased by approximately 34% near the failure curvature compared with values extrapolated from the initial stiffness of T300-1k/HexPly913 laminates. Similarly, Gamage [7] reported an average reduction of about 32% in bending moment relative to the extrapolated initial stiffness for laminates manufactured using the same carbon fibre but bonded with a different epoxy resin (PMT-F4) under CBT. Notably, the initial bending stiffness obtained from the CBT experiments, 39.76 ± 3.92 Nmm, is in close agreement with the value reported by Mallikarachchi and Pellegrino, 37.55 ± 5.54 Nmm.

Figure 5.5 compares the moment–curvature responses predicted by tow-only in-phase numerical models with linear material properties (ML) and geometric non-linearity against the experimental results.

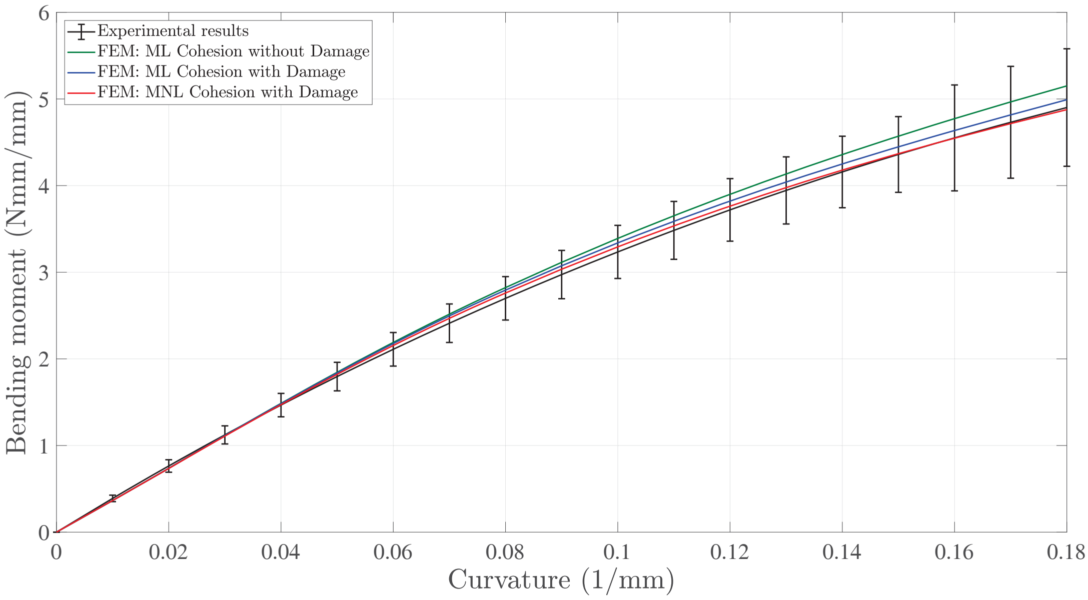

Figure 5.5: Moment-curvature response of numerical models with different tow interactions compared against experimental results

The reduction in bending stiffness of thin composite laminates at high curvatures arises from both geometrical and material non-linearities, as well as damage mechanisms. The model incorporating cohesive behaviour without damage criteria (ML Cohesion without Damage) assumes a perfectly elastic traction–separation relationship, thereby excluding tow delamination. Despite this, the model exhibits a reduction in bending stiffness with increasing curvature, indicating that non-linear geometrical effects, such as changes in tow cross-sectional area, reductions in tow thickness, and variations in tow undulation, are primary contributors to stiffness reduction at higher curvatures. When damage initiation and evolution are enabled (ML Cohesion with Damage), a pronounced drop in stiffness is observed beyond $\kappa_x = 0.07$ mm^{-1}, with detailed inspection revealing substantial relative slip between tows. This micro-slipping arises from cohesive failures that develop as the applied curvature increases, further contributing to the reduction in bending stiffness, as illustrated in Figure 5.6.

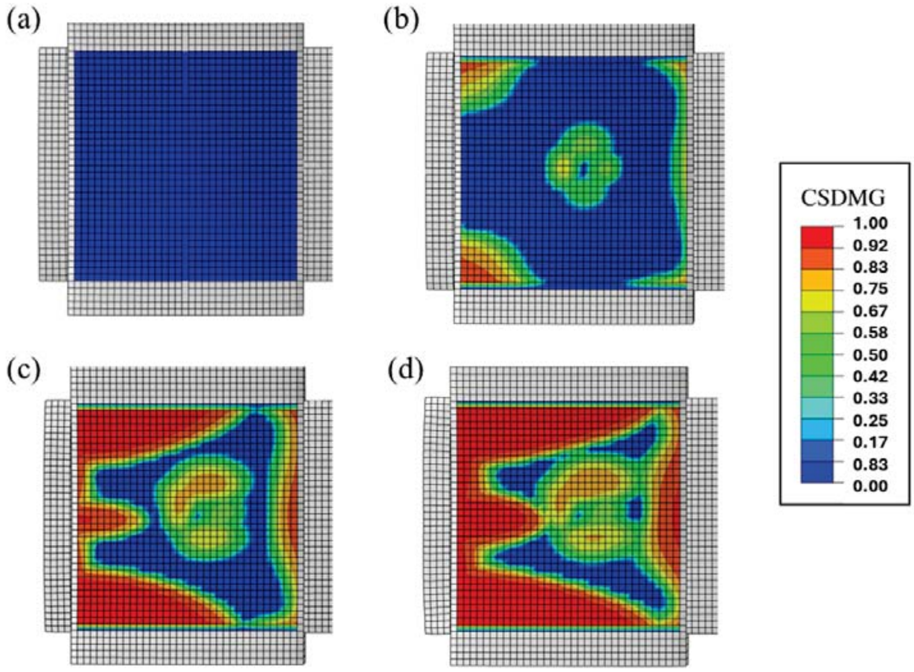

Figure 5.6: Damage variable for cohesive surfaces (CSDMG) at: (a) $\kappa_x = 0$, (b) $\kappa_x = 0.05$ mm^{-1}, (c) $\kappa_x = 0.1$ mm^{-1} and (d) $\kappa_x = 0.15$ mm^{-1}

The material non-linear model (MNL) closely replicates the mean experimental trend, emphasising the role of material non-linearity in stiffness reduction at high curvatures. In this model, the elastic modulus of carbon fibres increases under tensile strains and decreases under compressive strains. The divergence between linear and non-linear model predictions becomes apparent beyond $\kappa_x = 0.06$ mm^{-1}, primarily due to compression-induced softening. As the curvature increases, the neutral axis shifts towards the stiffer tensile side, reducing the effective thickness and consequently lowering the bending stiffness, D_{11}. Unlike linear bending, where tensile and compressive strains are symmetric, compressive strains can be up to 25% greater than tensile strains at high curvatures in thin composite laminates [51]. Together, these results demonstrate that stiffness reduction in woven fibre laminates under large curvatures is governed by a combination of geometrical effects, tow-scale damage mechanisms, and material non-linearity.

Figure 5.7 compares the variations of D_{11} with experimental data for tow-only in-phase models. Although the numerical moment–curvature responses closely match the experimental results, the D_{11} variations indicate an under-prediction of the initial bending stiffness for tow-only models.

This arises because, despite perfect contact between tows within each ply,

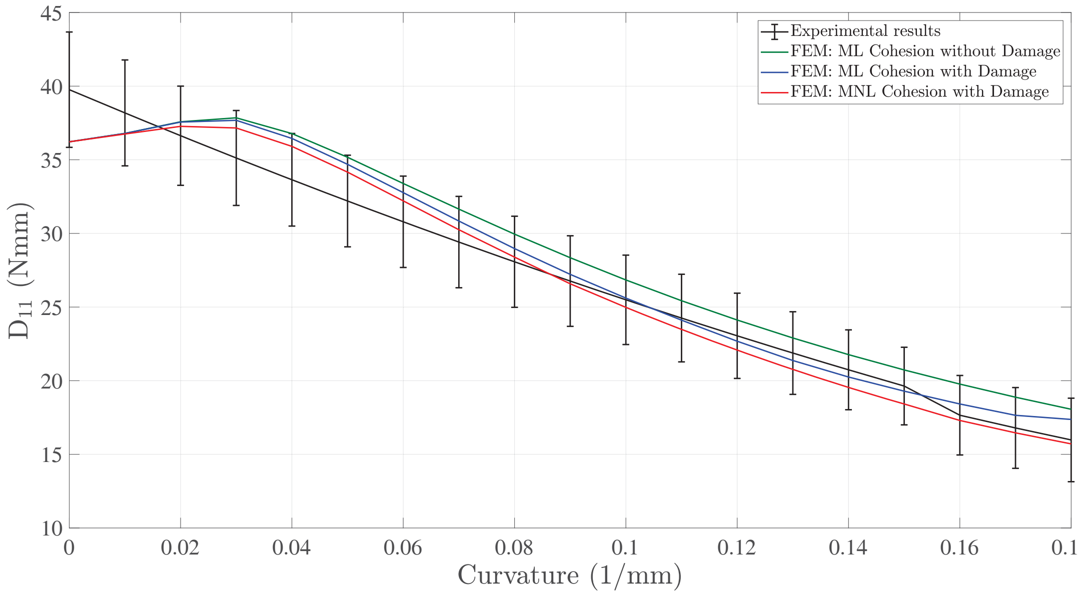

Figure 5.7: D_{11} variations of numerical models with different tow interactions compared against experimental results

there are only four contact points between the upper and lower plies, causing the two plies to behave almost independently. This observation highlights the importance of modelling the resin between plies, as it constrains the relative movement of one ply with respect to the other.

5.3 Moment-Curvature Response of In-Phase Resin Model

As discussed in Section 4.4, in addition to the 12 cohesive interactions in the tow-only model, eight additional interactions were defined for the resin model. These include four interactions between the lower surface of the upper ply and the upper surface of the resin, and four interactions between the upper surface of the lower ply and the lower surface of the resin. The corresponding moment–curvature response is shown in Figure 5.8.

It is worth noting that, with the inclusion of the resin, the predicted initial bending stiffness is 39.9 Nmm, closely matching the experimental value of 39.76 ± 3.92 Nmm [7], whereas the tow-only model predicted 36.2 Nmm. This emphasises the importance of modelling the resin for a more realistic representation.

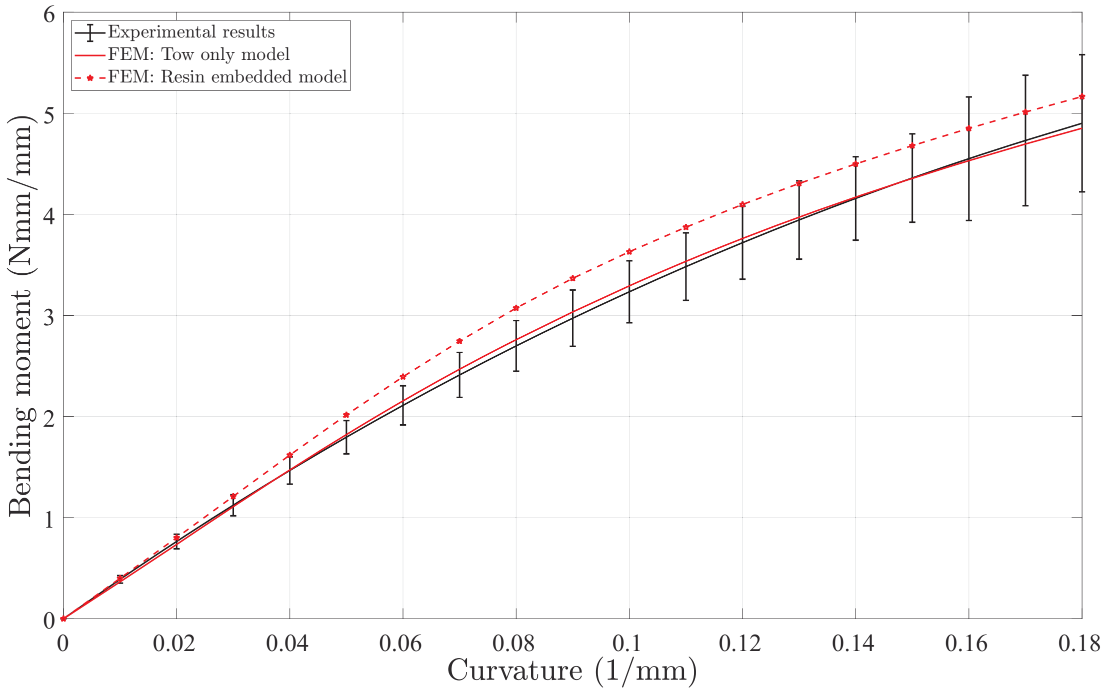

Figure 5.8: Comparison of moment-curvature responses of tow-only and resin-embedded numerical models

5.4 Moment-Curvature Response of Out-of-Phase Model

As discussed in Section 3.1, there are infinitely many possible configurations for stacking the plies, depending on the phase difference between the top and bottom ply. Although care was taken to maintain a fibre in-phase arrangement during manufacturing, deviations can occur, particularly when impregnating the resin under high pressures. Consequently, it is important to consider alternative phase angles, such as the fibre out-of-phase arrangement. The corresponding moment–curvature variations for the fibre in-phase and fibre out-of-phase configurations are shown in Figure 5.8 for resin-embedded models.

5.5 Variation of Moment–Curvature Response with Fibre Volume Fraction

Until now, the fibre volume fraction used to calculate the homogenised material properties of the tows has been 0.62, which corresponds to the experimentally measured value obtained using a weight-based approach. Based on this fibre volume fraction, the resin volume fraction in the laminate would be 0.38. However, it is important to note that resin present outside the tows, in addition to the resin contained within the tows, as illustrated in Figure 5.10.

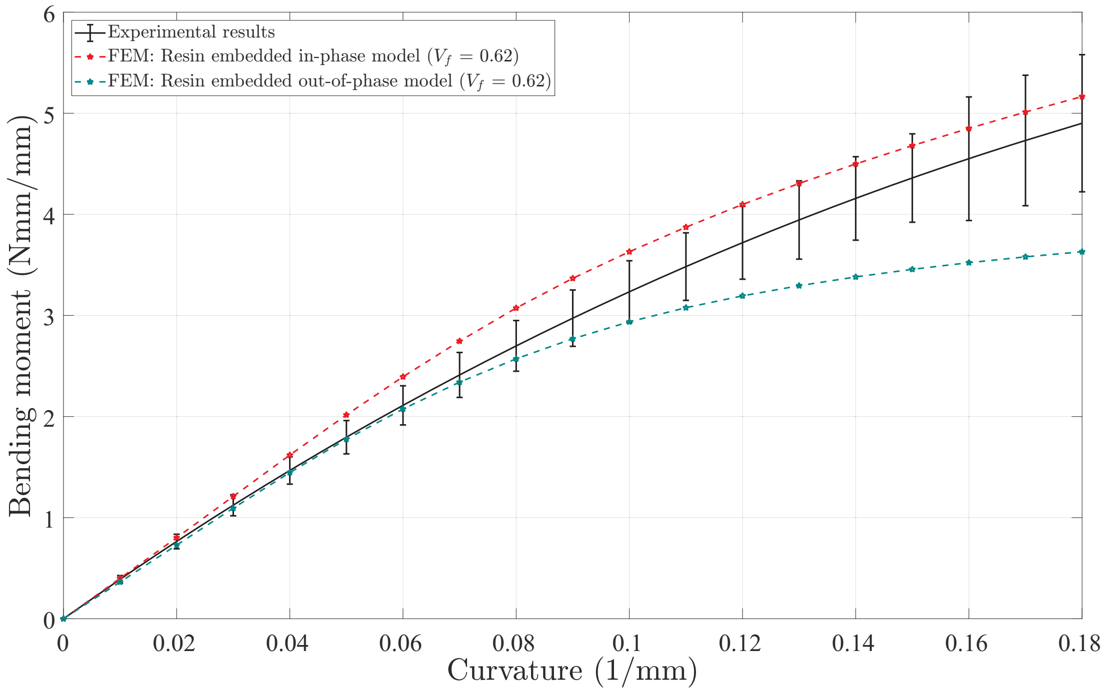

Figure 5.9: Comparison of moment-curvature responses of in-phase and out-of-phase numerical models

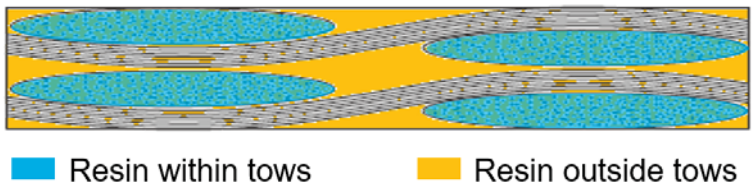

Figure 5.10: Comparison of moment-curvature responses of in-phase and out-of-phase numerical models

The resin volume fraction of 0.38 in the laminate represents the total resin, comprising both the resin contained within the tows and the resin outside the tows. Consequently, the resin volume fraction within a tow is less than the total resin volume fraction, meaning that the fibre volume fraction within a tow is higher than the overall fibre volume fraction of the laminate. Since the weight of the resin used during manufacturing is known, it is possible to estimate the maximum fibre volume fraction achievable within a tow, which was determined to be 0.68. A separate set of numerical simulations was then conducted using this increased fibre volume fraction, and the resulting moment–curvature responses are presented in Figure 5.11.

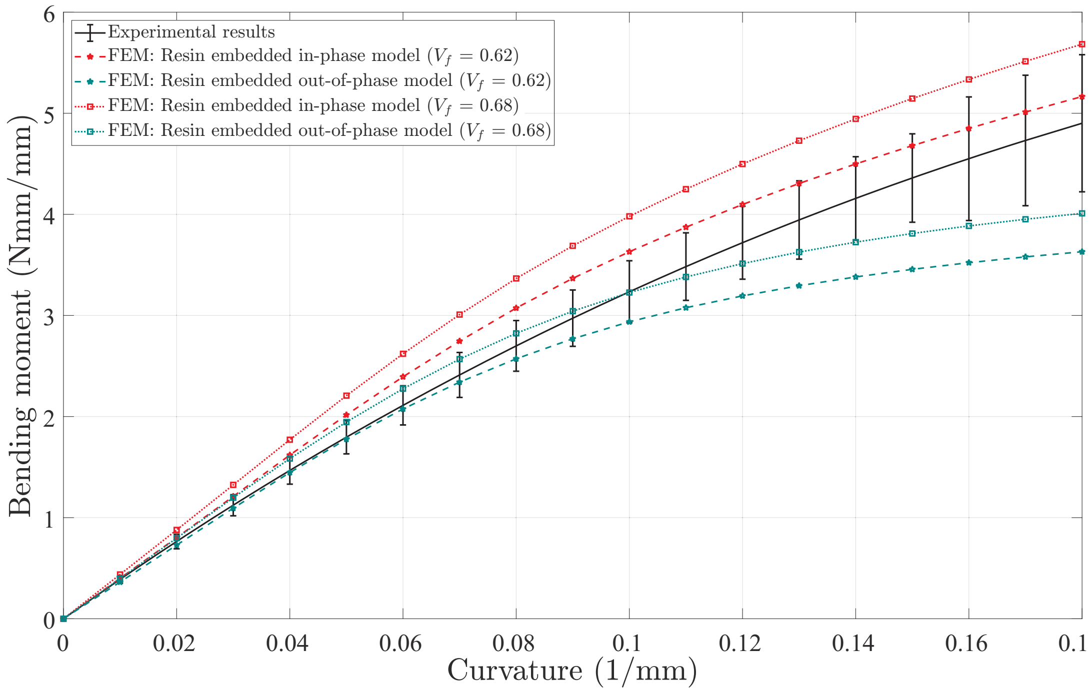

Figure 5.11: Comparison of moment-curvature responses of in-phase and out-of-phase numerical models with different fibre volume fractions

5.6 Analysis of Axial Behaviour

Axial responses were extracted up to failure strains under tensile loading for composite laminates reported in the literature [6, 26]. As shown in Figure 5.12, the numerical models successfully capture the reported tensile hardening behaviour, demonstrating that the constitutive model accurately represents the strain-dependent stiffening of the carbon fibres. This tensile hardening also directly influences the laminate bending response, as it increases the effective stiffness in tension-dominated bending regions. Consequently, incorporating this material non-linearity in the models allows for a more realistic prediction of the moment–curvature response, particularly at higher curvatures where compressive softening and tensile hardening effects produce asymmetry in the strain distribution across the laminate thickness.

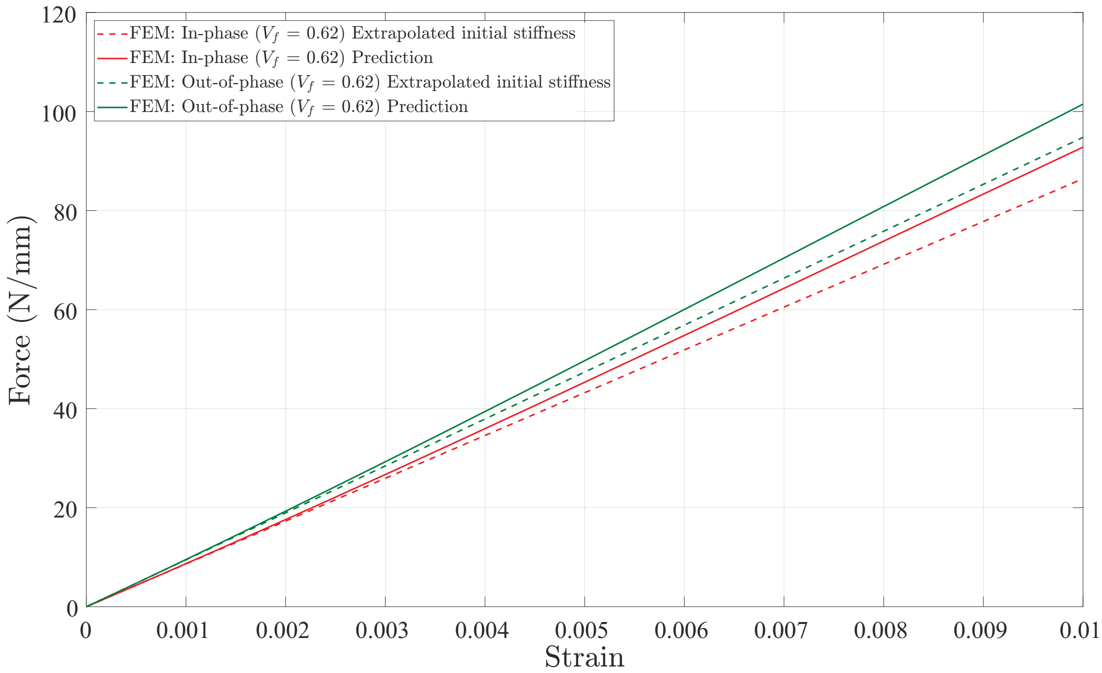

Figure 5.12: Comparison of axial responses of in-phase and out-of-phase numerical models

Chapter 6

Conclusions and Future Work

6.1 Conclusions

The present study developed a comprehensive numerical framework to investigate the non-linear bending behaviour of ultra-thin two-ply plain-weave composite laminates. Using RUC-based homogenisation approach, both geometric and material non-linearities, as well as cohesive interface interactions, were incorporated to accurately capture the experimentally observed reduction in bending stiffness at large curvatures.

The primary objective of this work was to reproduce the geometrically non-linear moment–curvature response of woven composites and identify the mechanisms responsible for stiffness reduction under high-curvature bending. To achieve this, a multi-scale finite element model was developed, integrating a precise geometric representation of the woven architecture, cohesive traction–separation behaviour at tow contact interfaces, a strain-dependent constitutive law to describe the material non-linearity of the fibre tows, and geometric non-linearity associated with large deformations.

The numerical results showed strong agreement with experimental data across the entire curvature range investigated. The model accurately predicted the progressive reduction in bending stiffness with increasing curvature, validating the hypothesis that this degradation arises from the combined influence of inter-tow interaction, material non-linearity, and geometric deformation effects. Specifically, analyses revealed that at moderate curvatures, geometric factors such as tow flattening, changes in cross-sectional area, and the shift of the neutral axis dominate the stiffness reduction. At higher curvatures, cohesive damage and micro-slipping between adjacent tows become the principal contributors.

Including resin layers between plies was shown to be essential for accurate stiffness prediction. The resin not only increased the number of contact interfaces but also effectively constrained inter-ply motion, thereby enhancing the model's ability to replicate the experimentally measured initial stiffness. A comparative study of fibre in-phase and out-of-phase stacking arrangements further highlighted the sensitivity of bending stiffness to ply alignment. The results indicate that even slight variations in ply positioning during manufacturing can lead to noticeable differences in mechanical response, an important consideration for the design and quality control of ultra-thin woven laminates.

Overall, the outcomes of this study confirm that the proposed RUC-based non-linear homogenisation framework is a robust and reliable tool for simulating the complex bending behaviour of woven composites. The model not only reproduces experimental results with high accuracy but also provides mechanistic insights into the factors governing stiffness degradation. Furthermore, the approach allows for the extraction of homogenised laminate stiffness terms, which can be used to populate the ABD stiffness matrix essential for macro-scale design and analysis of deployable composite structures.

6.2 Future Work

Although the present work successfully captures the non-linear bending response of ultra-thin woven laminates, several avenues exist to further enhance the model's predictive capability and broaden its applicability.

First, a comprehensive parametric study could be undertaken to quantify the relative contributions of individual mechanisms, such as fibre volume fraction, resin pocket thickness and ply misalignment, to the overall stiffness reduction.

Second, integrating the homogenised stiffness parameters obtained from this study into macro-scale deployable structure simulations would bridge the gap between material-level characterisation and system-level design. Such multi-scale integration would enable accurate prediction of folding, deployment, and shape recovery in ultra-thin composite structures, paving the way for the development of lighter, more reliable, and efficient space systems.

References

[1] D. Adams and M. Mobrem, "Marsis antenna flight deployment anomaly and resolution," in *47th AIAA/ASME/ASCE/AHS/ASC Structures, Structural Dynamics, and Materials Conference 14th AIAA/ASME/AHS Adaptive Structures Conference 7th*, 2006, p. 1684.

[2] H. Mallikarachchi and S. Pellegrino, "Design of ultrathin composite self-deployable booms," *Journal of Spacecraft and Rockets*, vol. 51, no. 6, pp. 1811–1821, 2014.

[3] M. Sakovsky and S. Pellegrino, "Closed cross-section dual-matrix composite hinge for deployable structures," *Composite Structures*, vol. 208, pp. 784–795, 2019.

[4] S. Wang, M. Schenk, S. Jiang, and A. Viquerat, "Blossoming analysis of composite deployable booms," *Thin-Walled Structures*, vol. 157, p. 107098, 2020.

[5] K. Wilkie, "The nasa advanced composite solar sail system flight demonstration: A technology pathfinder for practical smallsat solar sailing," *35th Annual Small Satellite Conference*, 2021.

[6] H. Mallikarachchi and S. Pellegrino, "Failure criterion for two-ply plain-weave cfrp laminates," *Journal of Composite Materials*, vol. 47, no. 11, pp. 1357–1375, 2013.

[7] E. S. Gamage, "Multiscale modelling of ultra-thin woven fibre composites under large curvatures," Master's thesis, University of Moratuwa, 2025.

[8] S. Timoshenko and S. Woinowsky-Krieger, *Theory of plates and shells*. McGraw-Hill Book Company, 1959.

[9] B. Le Page, F. Guild, S. Ogin, and P. Smith, "Finite element simulation of woven fabric composites," *Composites Part A: Applied Science and Manufacturing*, vol. 35, no. 7-8, pp. 861–872, 2004.

[10] R. A. Naik, "Failure analysis of woven and braided fabric reinforced composites," *Journal of Composite Materials*, vol. 29, no. 17, pp. 2334–2363, 1995.

[11] R. L. Karkkainen and B. V. Sankar, "A direct micromechanics method for analysis of failure initiation of plain weave textile composites," *Composites Science and Technology*, vol. 66, no. 1, pp. 137–150, 2006.

[12] Ö. Soykasap, "Micromechanical models for bending behavior of woven composites," *Journal of Spacecraft and Rockets*, vol. 43, no. 5, pp. 1093–1100, 2006.

[13] A. Le, S. Nimbalkar, N. Zobeiry, and S. Malek, "An efficient multi-scale approach for viscoelastic analysis of woven composites under bending," *Composite Structures*, vol. 292, p. 115698, 2022.

[14] J. Gao, W. Chen, B. Yu, P. Fan, B. Zhao, J. Hu, D. Zhang, G. Fang, and F. Peng, "A multi-scale method for predicting abd stiffness matrix of single-ply weave-reinforced composite," *Composite structures*, vol. 230, p. 111478, 2019.

[15] B. Wang, J. Zhu, S. Zhong, W. Liang, and C. Guan, "Space deployable mechanics: A review of structures and smart driving," *Materials & Design*, vol. 237, p. 112557, 2024.

[16] T. W. Murphey, W. Francis, B. Davis, and J. M. Mejia-Ariza, "High strain composites," in *2nd AIAA spacecraft structures conference*, 2015, p. 0942.

[17] C. Mallikarachchi, "Thin-walled composite deployable booms with tape-spring hinges," Ph.D. dissertation, University of Cambridge, 2011.

[18] A. H. Sharma, T. Rose, A. Seamone, T. W. Murphey, and F. Lopez Jimenez, "Analysis of the column bending test for large curvature bending of high strain composites," in *AIAA scitech 2019 forum*, 2019, p. 1746.

[19] T. W. Murphey, M. E. Peterson, and M. M. Grigoriev, "Large strain four-point bending of thin unidirectional composites," *Journal of Spacecraft and Rockets*, vol. 52, no. 3, pp. 882–895, 2015.

[20] A. Schlothauer, G. A. Pappas, and P. Ermanni, "Material response and failure of highly deformable carbon fiber composite shells," *Composites Science and Technology*, vol. 199, p. 108378, 2020.

[21] X. Ji, A. M. Khatri, E. S. Chia, R. K. Cha, B. T. Yeo, S. C. Joshi, and Z. Chen, "Multi-scale simulation and finite-element-assisted computation of elastic properties of braided textile reinforced composites," *Journal of Composite Materials*, vol. 48, no. 8, pp. 931–949, 2014.

[22] J. Mao, X. Sun, M. Ridha, V. Tan, and T. Tay, "A modeling approach across length scales for progressive failure analysis of woven composites," *Applied Composite Materials*, vol. 20, no. 3, pp. 213–231, 2013.

[23] M. G. Geers, V. G. Kouznetsova, and W. Brekelmans, "Multi-scale computational homogenization: Trends and challenges," *Journal of computational and applied mathematics*, vol. 234, no. 7, pp. 2175–2182, 2010.

[24] S. Herath, "Multiscale modelling and material design of woven textiles using gaussian processes," *Acta Mechanica*, vol. 233, no. 1, pp. 317–341, 2022.

[25] C. Wanasinghe, S. Dharmawansha, N. Ariyasinghe, P. Ranatunga, S. Herath, C. Mallikarachchi, and D. Meddage, "Multiscale modelling and explainable ai for predicting mechanical properties of carbon fibre woven composites with parametric microscale and mesoscale configurations," *Composite Structures*, p. 119282, 2025.

[26] A. Kueh and S. Pellegrino, "Triaxial weave fabric composites," Department of Engineering, University of Cambridge, Tech. Rep., 2007.

[27] Y. Yapa and H. Mallikarachchi, "Predicting non-linear bending behaviour of thin woven fibre composites," *Society of Structural Engineers, Sri Lanka-Annual session 2017*, 2017.

[28] H. S. Wijesuriya, "Predicting non-linear bending behaviour of ultra-thin woven fibre composites," Master's thesis, University of Moratuwa, 2019.

[29] S. Nadarajah, M. Jayasekara, and C. Mallikarachchi, "Nonlinear bending response of two-ply plain woven carbon fibre composites," in *2019 Moratuwa Engineering Research Conference (MERCon)*. IEEE, 2019, pp. 147–151.

[30] Ö. Soykasap, "Analysis of tape spring hinges," *International Journal of Mechanical Sciences*, vol. 49, no. 7, pp. 853–860, 2007.

[31] Torayca, *Technical Data Sheet No. CFA-001, T300 Data Sheet*, Toray Industries, Inc. [Online]. Available: https://www.toraycma.com/resources/data-sheets/

[32] PATZ, *Technical Data Sheet PMT-F4*, PATZ Materials and Technologies. [Online]. Available: https://www.patzmandt.com/systems

[33] K. Naito, Y. Tanaka, and J.-M. Yang, "Transverse compressive properties of polyacrylonitrile (pan)-based and pitch-based single carbon fibers," *Carbon*, vol. 118, pp. 168–183, 2017.

[34] S. Wong, A. Pierlot, A. Abbott, and J. Schutz, "Direct measurement of the transverse modulus of carbon fibres," *Experimental Mechanics*, vol. 62, no. 5, pp. 769–778, 2022.

[35] R. M. Jones, *Mechanics of composite materials*. CRC press, 2018.

[36] I. M. Daniel, O. Ishai, I. M. Daniel, and I. Daniel, *Engineering mechanics of composite materials*. Oxford university press New York, 1994, vol. 3.

[37] S. C. Quek, A. M. Waas, K. W. Shahwan, and V. Agaram, "Analysis of 2d triaxial flat braided textile composites," *International Journal of Mechanical Sciences*, vol. 45, no. 6-7, pp. 1077–1096, 2003.

[38] G. Sanford, A. Biskner, and T. Murphey, "Large strain behavior of thin unidirectional composite flexures," in *51st AIAA/ASME/ASCE/AHS/ASC Structures, Structural Dynamics, and Materials Conference 18th AIAA/ASME/AHS Adaptive Structures Conference 12th*, 2010, p. 2698.

[39] T. W. Murphey, "Large strain composite materials in deployable space structures," in *17th International Conference on Composite Materials*, vol. 28. The British Composites Society Edinburgh, United Kingdom, 2009.

[40] J. Hughes, "Strength and modulus of current carbon fibres," *Carbon*, vol. 24, no. 5, pp. 551–556, 1986.

[41] K. Naito, Y. Tanaka, J. Yang, and Y. Kagawa, "Tensile and flexural properties of single carbon fibres," in *ICCM-17-17th International Conference on Composite Materials*. International Committee on Composite Materials, 2009.

[42] A. Schlothauer, D. Cueni, G. A. Pappas, and P. Ermanni, "Effects of fiber non-linearity and matrix type on the realization of foldable structures," in *AIAA Scitech 2021 Forum*, 2021, p. 0086.

[43] G. Curtis, J. Milne, and W. Reynolds, "Non-hookean behaviour of strong carbon fibres," *Nature*, vol. 220, no. 5171, pp. 1024–1025, 1968.

[44] A. CRASTO and R. KIM, "Nonlinear stress-strain behavior in advanced fibers and composites," in *International SAMPE Symposium and Exhibition, 36 th, San Diego, CA*, 1991, pp. 1649–1663.

[45] I. M. Djordjevic, D. R. Sekulić, and M. M. Stevanović, "Non-linear elastic behaviour of carbon fibres of different structural and mechanical characteristic," *Journal of the Serbian Chemical Society*, vol. 72, no. 5, pp. 513–521, 2007.

[46] V. Keryvin, A. Marchandise, P.-Y. Mechin, and J.-C. Grandidier, "Determination of the longitudinal non linear elastic behaviour and compressive strength of a cfrp ply by bending tests on laminates," *Composites Part B: Engineering*, vol. 187, p. 107863, 2020.

[47] V. Keryvin, A. Marchandise, and J.-C. Grandidier, "Non-linear elastic longitudinal behaviour of continuous carbon fibres/epoxy matrix composite laminae: Material or geometrical feature?" *Composites Part B: Engineering*, vol. 247, p. 110329, 2022.

[48] A. Harihara Sharma, T. J. Rose, N. Bearns, T. W. Murphey, and F. López Jiménez, "Analysis of geometric and material nonlinearity in the column bending test," *AIAA Journal*, vol. 62, no. 4, pp. 1300–1310, 2024.

[49] T. W. Murphey, G. E. Sanford, and M. M. Grigoriev, "Nonlinear elastic constitutive modeling of large strains in thin carbon fiber composite flexures," in *16th International conference on composite structures, Porto, Portugal*, 2011.

[50] V. Keryvin and A. Marchandise, "The non-linear elasticity of unidirectional continuous carbon fibre-reinforced composites and of carbon fibres," *Materials*, vol. 17, no. 1, p. 34, 2023.

[51] K. Ubamanyu and S. Pellegrino, "Nonlinear behavior of im7 carbon fibers in compression leads to bending nonlinearity of high-strain composites," in *AIAA Scitech 2023 Forum*, 2023, p. 0580.

[52] N. Gowrikanthan, M. Jayasekara, C. Mallikarachchi, and S. Herath, "Effects of tow arrangements on the homogenized response of carbon fiber woven composites," *Composite Structures*, vol. 300, p. 116081, 2022.

[53] H. Mallikarachchi, "Predicting mechanical properties of thin woven carbon fiber reinforced laminates," *Thin-Walled Structures*, vol. 135, pp. 297–305, 2019.

[54] J.-K. Kim and M.-L. Sham, "Impact and delamination failure of woven-fabric composites," *Composites Science and Technology*, vol. 60, no. 5, pp. 745–761, 2000.

[55] D. Wilkins, J. Eisenmann, R. Camin, W. Margolis, and R. Benson, "Characterizing delamination growth in graphite-epoxy," in *Damage in composite materials: basic mechanisms, accumulation, tolerance, and characterization*. ASTM International, 1982.

[56] J. G. Funk and G. F. Sykes, "The effects of radiation on the interlaminar fracture toughness of a graphite/epoxy composite," *Composites Technology and Research*, vol. 8, no. 3, pp. 92–97, 1986.

[57] J. G. Funk and J. W. Deaton, "The interlaminar fracture toughness of woven graphite/epoxy composites," NASA, Tech. Rep., 1989.

[58] A. Kueh and S. Pellegrino, "Abd matrix of single-ply triaxial weave fabric composites," in *48th AIAA/aSME/ASCE/AHS/aSC structures, structural dynamics, and materials conference*, 2007, p. 2161.

Appendix A

Scripts for Pre-Processing

A.1 Python code used in TexGen textile modelling software

```
% Read the textile
textile = GetTextile('Textile Name')

% Read the Yarn (Tow)
yarn = textile.GetYarn(Tow Number)

% Setting the resolution
yarn.SetResolution(Number of nodes along the tow path,
Number of nodes along the circumference of the
cross-section)

% Set the cross section
section = CSectionPowerEllipse(width, thickness, power)

% Setting the number of mesh layers through thickness
section.SetSectionMeshLayers(number of mesh layers needed)
yarn.AssignSection(CYarnSectionConstant(section))
```

Appendix B

Scripts Used in Abaqus

B.1 Edited output requests in Abaqus **.inp* file

```
** OUTPUT REQUESTS
**
*Restart, write, frequency=0
**
** FIELD OUTPUT: F-Output-1
**
*Output, field
*Node Output
CF, RF, U
*Element Output, directions=YES
LE, PE, PEEQ, PEMAG, S
*Contact Output
CDISP, CSDMG, CSTRESS
**
** HISTORY OUTPUT: H-Output-1
**
*Output, history, time interval=0.05, variable=PRESELECT
*Node Print, Nset=NODE_Y1_1, Summary=No, freq=1
RF
*Node Print, Nset=NODE_Y2_1, Summary=No, freq=1
RF
*Node Print, Nset=NODE_X1_1, Summary=No, freq=1
RF
*Node Print, Nset=NODE_X2_1, Summary=No, freq=1
```

```
RF
*Node Print, Nset=NODE_Y1_2, Summary=No, freq=1
RF
*Node Print, Nset=NODE_Y2_2, Summary=No, freq=1
RF
*Node Print, Nset=NODE_X1_2, Summary=No, freq=1
RF
*Node Print, Nset=NODE_X2_2, Summary=No, freq=1
RF
.
.
.
*Node Print, Nset=NODE_Y1_34, Summary=No, freq=1
RF
*Node Print, Nset=NODE_Y2_34, Summary=No, freq=1
RF
*Node Print, Nset=NODE_X1_34, Summary=No, freq=1
RF
*Node Print, Nset=NODE_X2_34, Summary=No, freq=1
RF
*Node Print, Nset=RP_R_1_1, Summary=No, freq=1
U
*Node Print, Nset=RP_P_1_1, Summary=No, freq=1
U
*Node Print, Nset=RP_R_2_1, Summary=No, freq=1
U
*Node Print, Nset=RP_P_2_1, Summary=No, freq=1
U
*Node Print, Nset=RP_S_1_1, Summary=No, freq=1
U
*Node Print, Nset=RP_Q_1_1, Summary=No, freq=1
U
*Node Print, Nset=RP_S_2_1, Summary=No, freq=1
U
*Node Print, Nset=RP_Q_2_1, Summary=No, freq=1
U
```

```
*Node Print, Nset=RP_R_1_2, Summary=No, freq=1
U
*Node Print, Nset=RP_P_1_2, Summary=No, freq=1
U
*Node Print, Nset=RP_R_2_2, Summary=No, freq=1
U
*Node Print, Nset=RP_P_2_2, Summary=No, freq=1
U
*Node Print, Nset=RP_S_1_2, Summary=No, freq=1
U
*Node Print, Nset=RP_Q_1_2, Summary=No, freq=1
U
*Node Print, Nset=RP_S_2_2, Summary=No, freq=1
U
*Node Print, Nset=RP_Q_2_2, Summary=No, freq=1
U
.
.
.
*Node Print, Nset=RP_R_1_34, Summary=No, freq=1
U
*Node Print, Nset=RP_P_1_34, Summary=No, freq=1
U
*Node Print, Nset=RP_R_2_34, Summary=No, freq=1
U
*Node Print, Nset=RP_P_2_34, Summary=No, freq=1
U
*Node Print, Nset=RP_S_1_34, Summary=No, freq=1
U
*Node Print, Nset=RP_Q_1_34, Summary=No, freq=1
U
*Node Print, Nset=RP_S_2_34, Summary=No, freq=1
U
*Node Print, Nset=RP_Q_2_34, Summary=No, freq=1
U
*End Step
```

B.2 USDFLD subroutine

```
      SUBROUTINE USDFLD(FIELD,STATEV,PNEWDT,DIRECT,T,CELENT,
     1
TIME,DTIME,CMNAME,ORNAME,NFIELD,NSTATV,NOEL,NPT,
     2
LAYER,KSPT,KSTEP,KINC,NDI,NSHR,COORD,JMAC,JMATYP,
     3      MATLAYO,LACCFLA)

C     --- Include Abaqus parameters ---
      INCLUDE 'ABA_PARAM.INC'

C     --- Variable definitions ---
      CHARACTER*80 CMNAME, ORNAME
      CHARACTER*3  FLGRAY(15)

      DIMENSION FIELD(NFIELD), STATEV(NSTATV), DIRECT(3,3)
      DIMENSION T(3,3), TIME(2)
      DIMENSION ARRAY(15), JARRAY(15)
      DIMENSION JMAC(*), JMATYP(*), COORD(*)

C                         GET CURRENT TOTAL STRAIN
C     GETVRM requests variable E --> total strain tensor.
C     Results are stored in ARRAY() in Abaqus ordering.

      CALL GETVRM('E', ARRAY, JARRAY, FLGRAY, JRCD,
     1              JMAC, JMATYP, MATLAYO, LACCFLA)

C     Extract strain component E11
      E11 = ARRAY(1)

C     Assign strain as field variable 1
      FIELD(1) = E11

      RETURN
      END
```

Appendix C

Scripts for Post-Processing

C.1 Python code used to extract the output from Abaqus **.dat* file

```
import os
import re

job_name = 'Kxx'
output_directory = 'Tests'
if not os.path.exists(output_directory):
    os.makedirs(output_directory)

with open(job_name + '.dat', 'r') as infile:
    lines = infile.readlines()

time_steps = [5.000, 0.10, 0.15, 0.20, 0.25, 0.30, 0.35,
0.40, 0.45, 0.50, 0.55, 0.60, 0.65, 0.70, 0.75, 0.80,
0.85, 0.90, 0.95, 1.00]

for t in time_steps:
    # regex pattern with 3 decimal places, flexible spaces
    pattern = re.compile(r'TOTAL TIME COMPLETED\s+' +
    re.escape(f'{t:.2f}'))

    start_index = None

    for idx, line in enumerate(lines):
        if pattern.search(line):
```

```
            start_index = idx
            break

    if start_index is None:
        continue

    end_index = start_index + 3681
    extracted = lines[start_index : min(end_index,
    len(lines))]


    if t == 5.000:
        output_filename = f'Kxx_{0.05}.txt'

    else:
        output_filename = f'Kxx_{t:.2f}.txt'

    output_path = os.path.join(output_directory,
    output_filename)
    with open(output_path, 'w') as outfile:
        outfile.writelines(extracted)
```

C.2 MATLAB code used to calculate ABD matrix

```
L = 2.88;

Vf = []; % Virtual force matrix
Vd = []; % Virtual displacement matrix

S1Q1 = [0.15,0.206577,0.241774,0.275556,0.308905,0.342059,
0.375104,0.40808,0.44101,0.473904,0.539618,0.539618,
0.572446,0.605258,0.638057,0.670843,0.703617,0.736383,
0.769157,0.801943,0.834742,0.867554,0.900382,0.933228,
0.966096,0.99899,1.03192,1.0649,1.09794,1.13109,1.16444,
1.19823,1.23342,1.29]; % X coordinates of Q1S1 nodes
```

```
S2Q2 = [1.59,1.64658,1.68177,1.71556,1.74891,1.78206,
1.8151,1.84808,1.88101,1.9139,1.94677,1.97962,2.01245,
2.04526,2.07806,2.11084,2.14362,2.17638,2.20916,2.24194,
2.27474,2.30755,2.34038,2.37323,2.4061,2.43899,2.47192,
2.5049,2.53794,2.57109,2.60444,2.63823,2.67342,2.73];
% X coordinates of Q2S2 nodes

R1P1 = fliplr(S1Q1); % Y coordinates of P1R1 nodes
R2P2 = fliplr(S2Q2); % Y coordinates of P2R2 nodes

for file = 0.2
    file_str = num2str(file, '%.2f');
    filename = ['Kxx_', file_str, '.txt'];

    [C1,C2,C3,C4,C5,C6,C7,C8,C9,C10,C11,C12]= textread
    (filename,'%s %s %s %s %s %s %s %s %s %s %s %s');

    Data=[C2 C3 C4 C5 C6 C7];

    NRF = []; % Nodal reaction forces
    RF = []; % All reaction forces

    Line_no = 6;
    a = 1;

        while Line_no < 547

        i = ceil((Line_no -3)/16);

        Y1 = [1/L 0 0 0 0 0;
        0 1/L 0 0 0 0;
        0 0 -1/(L*R1P1(1,i)) 0 0 0;
        0 0 0 -1/L 0 0;
        0 0 0 0 1/L 0;
        0 0 0 0 0 1];
```

```
Y2 = [1/L 0 0 0 0 0;
0 1/L 0 0 0 0;
0 0 -1/(L*R2P2(1,i)) 0 0 0;
0 0 0 -1/L 0 0;
0 0 0 0 1/L 0;
0 0 0 0 0 1];

X1 = [1/L 0 0 0 0 0;
0 1/L 0 0 0 0;
0 0 -1/(L*S1Q1(1,i)) 0 0 0;
0 0 0 -1/L 0 0;
0 0 0 0 1/L 0;
0 0 0 0 0 1];

X2 = [1/L 0 0 0 0 0;
0 1/L 0 0 0 0;
0 0 -1/(L*S2Q2(1,i)) 0 0 0;
0 0 0 -1/L 0 0;
0 0 0 0 1/L 0;
0 0 0 0 0 1];

NRF(:,1) = str2double(Data(Line_no,:));

if rem(a,4)==1
    NRF = Y1*NRF;

elseif rem(a,4)==2
    NRF = Y2*NRF;

elseif rem(a,4)==3
    NRF = X1*NRF;

else
    NRF = X2*NRF;

end
```

```
        RF = [RF; NRF; -NRF];

        Line_no = Line_no + 4;
        a = a + 1;

        end

        Vf =[Vf RF];

    NUR = []; % Nodal displacements
    UR = []; % All displacements

    b = 550;

    while b < 1635

        NUR(:,1) = str2double(Data(b,:));
        UR = [UR; NUR];

        b = b + 4;
    end

    Vd = [Vd UR];

end

ABD_Matrix = transpose(Vd)*Vf/((L*0.2*file)^2)
```